Spring 2016

# Enhancing the Photovoltaic Efficiency of a Bulk Heterojunction Organic Solar Cell

Swapnil Ashok Sahare
swapnil.sahare854@topper.wku.edu

# ENHANCING THE PHOTOVOLTAIC EFFICIENCY OF A BULK HETEROJUNCTION ORGANIC SOLAR CELL

A Thesis
Presented to
The Faculty of the Department of Chemistry
Western Kentucky University
Bowling Green, Kentucky

In Partial Fulfillment
Of the Requirements for the Degree
Master of Science

By
Swapnil Sahare

May 2016

ENHANCING THE PHOTOVOLTAIC EFFICIENCY OF A BULK HETEROJUNCTION ORGANIC SOLAR CELL

Date Recommended 04/22/2016

H. P. Rathnayake

Dr. Hemali Rathnayake, Director of Thesis

Dr. Stuart Burris

Dr. Bangbo Yan

Dean, Graduate School

4/26/16

Date

I dedicate this thesis to my parents, Ashok Sahare and Late Sheela Sahare.

## ACKNOWLEDGMENTS

Fortunately, I have got tremendous support for the completion of this thesis from many people, without whom it would not have been possible. Firstly, I would like to thank Dr. Hemali Rathnayake for the continuous support and encouragement she has provided throughout this research. Her guidance was the most valuable asset I had during this period. During my course she has taught me many theories and instrumentation techniques. I will be forever indebted to Dr. Hemali for pushing me in right direction. I would like to give special thanks to her for critically correcting my thesis.

Next, I would like to thank Dr. Stuart Burris and Dr. Bangbo Yan for investing their valuable time in reading my thesis and helping me to make the required corrections. I appreciate all their patience and the guidance for the thesis and defense.

I express my gratitude towards Dr. John Andersland for providing valuable help on scanning electron microscope studies and thermal evaporation.

I am grateful towards Dr. Stuart Burris and Pauline Norris for their support on atomic force microscopy, towards Alicia Mc Daniel for backing up continuous supply of chemicals. I am also thankful towards Haley and all the faculty from department of chemistry at WKU for their valuable support.

I would like to specially thank Dr Ananthkrishnan, Aubrey and our entire research group who gave me continuous support throughout my research work.

# Table of Contents

ENHANCING THE PHOTOVOLTAIC EFFICIENCY OF A BULK HETEROJUNCTION ORGANIC SOLAR CELL

Swapnil Ashok Sahare May 2016 92 Pages

Directed by: Dr Hemali Rathnayake, Dr Stuart Burris and Dr Bangbo Yan

Department of Chemistry Western Kentucky University

Active layer morphology of polymer-based solar cells plays an important role in improving power conversion efficiency (PCE). In this thesis, the focus is to improve the device efficiency of polymer-based solar cells. In the first objective, active layer morphology of polymer-solar cells was optimized though a novel solvent annealing technique. The second objective was to explore the possibility of replacing the highly sensitive aluminum cathode layer with a low-cost and stable alternative, copper metal. Large scale manufacturing of these solar cells is also explored using roll-to-roll printing techniques.

Poly (3-hexylthiophene) (P3HT) and phenyl-C61-butyric acid methyl (PCBM) were used as the active layer blend for fabricating the solar cell devices using bulk heterojunction (BHJ), which is a blend of a donor polymer and an acceptor material. Blends of the donor polymer, P3HT and acceptor, PCBM were cast using spin coating and the resulting active layers were solvent annealed with dichlorobenzene in an inert atmosphere. Solvent annealed devices showed improved morphology with nano-phase segregation revealed by atomic force microscopy (AFM) analysis. The roughness of the active layer was found to be 6.5 nm. The nano-phase segregation was attributed to PCBM clusters and P3HT domains being arranged under the solvent annealing conditions. These test devices showed PCE up to 9.2 % with current density of 32.32 mA/cm$^2$, which is the highest PCE reported to date for a P3HT-PCBM based system.

Copper was deposited instead of the traditional aluminum for device fabrication. We were able to achieve similar PCEs with copper-based devices. Conductivity measurements were done on thermally deposited copper films using the two-probe method. Further, for these two configurations, PCE and other photovoltaic parameters were compared.

Finally, we studied new techniques of large scale fabrication such as ultrasonic spray coating, screen-printing, and intense pulse light sintering, using the facilities at the Conn Center for Renewable Energy Research at the University of Louisville. In this study, prototype devices were fabricated on flexible ITO coated plastics. Sintering greatly improved the conductivity of the copper nano-ink cathode layer. We will explore this technique's application to large-scale fabrication of solar cell devices in the future work.

# CHAPTER 1

# INTRODUCTION

## 1.1 Overview

Solar energy is an unarguably an endless source of energy, and researchers have been working on harvesting solar energy for electricity for a long time.[1] Photovoltaics, which convert solar energy to electricity by using the photovoltaic effect, are mainly divided into two types; inorganic and organic. Inorganic based solar cells have improved substantially over the last few decades.[2] As a major breakthrough, the first silicon (inorganic) based solar cell was developed in 1954 by Bell labs.[3] Since then, the power conversion efficiency (PCE) for silicon solar cells has been improved from 6% to 24%.[4] However, there are major limitations with these solar cells including the high cost of materials, environmental toxicity, heavy weight of the operating solar panels, high capital cost for commercialization, and complex fabrication processes.[2]

Organic solar cells (OSCs), on the other hand, have many advantages over inorganic solar cells. OSCs are cheap to produce due to the low cost of materials and easy fabrication processes. They are also flexible, robust, and lightweight. Organic solar cells mainly consist of small organic molecules or conducting polymers as a photoactive layer. Furthermore, these materials are easily fine-tuned through synthetic modifications to match the full absorption region of the solar spectrum.

Early in organic photovoltaics research, mimicking chlorophylls and employing them in solar cells was the first focus because of their effective light harvesting properties.[5] Later, with the development of novel light absorbing molecular and polymeric materials, OSC research has improved significantly.[6–9] The first polymer based

solar cell was developed in the 1980's with power conversion efficiency less than 0.1%.[10] Later, in 1995 the concept of a bulk heterojunction (BHJ) was introduced by Prof. Alan Heeger.[11]

The BHJ organic solar cell is a photovoltaic device which converts light into electricity using p- and n-type donor and acceptor organic molecules. The BHJ layer is a solid state mixture of two components (donor and acceptor) with nanoscale phase separation among the two components. Previous research has shown that power conversion efficiency can be improved by developing new donor-acceptor molecules and by controlling their morphology.[12–14] However, no one has yet to develop an effective method to control the morphology of a BHJ layer.[15]

Presently, the most widely used and stable BHJ solar cells are made from electron donor, poly(3-hexylthiophenes) (P3HT) and electron acceptor fullerene derivatives, in particularly phenyl-$C_{61}$-butyric acid methyl ester (PCBM).[16] P3HT is a conducting polymer with alternate single and double bonds. Similarly, PCBM is a fullerene (Bucky ball) derivative with $SP^2$ hybridized carbon atoms. The π-conjugation in these materials helps in effective charge transfer throughout the BHJ layer. These donor and acceptor materials are considered as the most promising materials for organic photovoltaics. Until now, BHJ solar cells with PCE greater than 5% have been reported using P3HT: PCBM as a donor-acceptor system.[17]

Finally, commercialization viability of solar cells depends upon three factors: cost, efficiency, and durability of cells. Therefore, further improvisation in the efficiency and stability is highly needed for organic solar cells to compete with their inorganic counterparts. Currently, P3HT:PCBM based cells can last up to 5000 hours of lifetime

with glass-on-glass encapsulation of devices.[18] However, these devices barely last up to 40-50 days in air.[19] Therefore, new methods should be developed to improve the durability of these devices in air.

### 1.2 General goal of the research

The research goal of this thesis is to make highly efficient and stable P3HT: PCBM based BHJ solar cells and to investigate the possibility of their fabrication on a large scale substrate. We have set following three objectives to achieve this goal:

1) The first objective of our research is optimizing the active layer morphology of P3HT:PCBM solar cells by developing a novel solvent annealing process. To do this, devices will be fabricated using BHJ device architecture and then devices will be subjected to a series of solvent annealing conditions under 1,2-dichlorobenzene vapors. Solvent annealing methods improve the morphology of the active layer, which is crucial to enhance the charge transport in BHJ solar cells and therefore it is directly proportional to the device performance.

2) The second objective of this research is to develop a cheaper and more stable cathode material to replace existing aluminum cathode in BHJ solar cells. Copper is a high work function metal and more stable compared to aluminum in air. Additionally, copper is more conductive and cheaper than aluminum. Hence, devices will be fabricated using copper as a cathode and their device performance will be evaluated.

3) Finally, third objective is to study fabrication parameters for large scale BHJ solar cells. To do this, a large scale prototype of a BHJ solar cell will be made using laboratory optimized parameters. Roll-to-roll fabrication techniques are known to rapidly fabricate low cost BHJ solar cells. Moreover, large-scale fabrication methods such as ultrasonic

spray, screen-printing and intense-pulse light (IPL) sintering are widely practiced for organic photovoltaics (OPVs) and electronics. This thesis describes various parameters obtained to fabricate large scale prototype of BHJ solar cell using these techniques.

**References**


(1) Mazzio, K. A.; Luscombe, C. K. Chem Soc Rev The future of organic photovoltaics. *Chem. Soc. Rev.* **2015**, *44* (1), 78–90.

(2) Mohammad Bagher, A. Comparison of Organic Solar Cells and Inorganic Solar Cells. *Int. J. Renew. Sustain. Energy* **2014**, *3* (3), 53.

(3) Blandford, R.; Watkins, M. This Month in Physics History: April 25, 1954: Bell Labs Demonstrates the First Practical Silicon Solar Cell. *APS News* **2009**.

(4) Green Martin, Emery Keith, Hishikawa Yoshihiro, Warta Wilhelm, D. D. Solar Cell Efficiency Table Ver. 47. *Prog. Photovolt Res. Appl.* **2015**, *15* (November 2015), 659–676.

(5) Kampas, Frank and Gouterman, M. Photovoltaic Properties of octaethylporphyrin and tetraethylporphyrin. *J. Phys. Chem.* **1977**, *81*, 690–695.

(6) Winder, C. Sensitization of low bandgap polymer bulk heterojunction solar cells. *Thin Solid Films* **2002**, *403-404*, 373–379.

(7) Zhang, F.; Bijleveld, J.; Perzon, E.; Tvingstedt, K.; Barrau, S.; Inganäs, O.; Andersson, M. R. High photovoltage achieved in low band gap polymer solar cells by adjusting energy levels of a polymer with the LUMOs of fullerene derivatives. *J. Mater. Chem.* **2008**, *18* (D), 5468.

(8) Pan, Z.; Gu, H.; Wu, M.; Li, Y.; Chen, Y. Graphene-based functional materials for organic solar cells. *Opt. Mater. Express* **2012**, *2* (6), 58–65.

(9) Gupta, A.; Armel, V.; Xiang, W.; Fanchini, G.; Watkins, S. E.; Macfarlane, D. R.; Bach, U.; Evans, R. a. The effect of direct amine substituted push-pull oligothiophene chromophores on dye-sensitized and bulk heterojunction solar cells performance. *Tetrahedron* **2013**, *69* (17), 3584–3592.

(10) Tang, C. W. A two-layer organic solar cell . *Appl. Phys. Lett.* , **1986**, *48* , 183–185.

(11) Yu, G.; Gao, J.; Hummelen, J. C.; Wudl, F.; Heeger, a. J. Polymer Photovoltaic Cells: Enhanced Efficiencies via a Network of Internal Donor-Acceptor Heterojunctions. *Science* **1995**, *270*, 1789–1791.

(12) Peet, J.; Kim, J. Y.; Coates, N. E.; Ma, W. L.; Moses, D.; Heeger, a J.; Bazan, G. C. Efficiency enhancement in low-bandgap polymer solar cells by processing with alkane dithiols. *Nat. Mater.* **2007**, *6*, 497–500.

(13) Schlenker, C. W.; Thompson, M. E. The molecular nature of photovoltage losses in organic solar cells. *Chem. Commun. (Camb).* **2011**, *47* (13), 3702–3716.

(14) Rio, Y.; Vazquez, P.; Palomares, E. Extended π-aromatic systems for energy conversion:: phthalocyanines and porphyrins in molecular solar cells. *J. Porphyr. Phthalocyanines* **2009**, *13* (4-5), 645–651.

(15) Heeger, A. J. 25th anniversary article: Bulk heterojunction solar cells: Understanding the mechanism of operation. *Adv. Mater.* **2014**, *26*, 10–28.

(16) Ge, N. An overview on P3HT : PCBM , the most efficient organic solar cell material so far . *Solid State Phys.* **2009**, 1, 1–11.

(17) Verploegen, E.; Miller, C. E.; Schmidt, K.; Bao, Z.; Toney, M. F. Manipulating the Morphology of P3HT–PCBM Bulk Heterojunction Blends with Solvent Vapor Annealing. *Chem. Mater.* **2012**, *24* (20), 3923–3931.

(18) Jorgensen, M.; Norrman, K.; Gevorgyan, S. a.; Tromholt, T.; Andreasen, B.; Krebs, F. C. Stability of polymer solar cells. *Adv. Mater.* **2012**, *24* (5), 580–612.

(19) Zhao, J.; Swinnen, A.; Van Assche, G.; Manca, J.; Vanderzande, D.; Van Mele, B. Phase diagram of P3HT/PCBM blends and its implication for the stability of morphology. *J. Phys. Chem. B* **2009**, *113* (6), 1587–1591.

# CHAPTER 2

# BACKGROUND

## 2.1 Need of a renewable energy

Currently, a major part of the world relies on conventional energy sources, including coal, natural gas, and oil. About 81 % of world total energy consumption is drawn from these sources. There are limited sources available, and they will soon end in future. Additionally, burning fossil fuels produces heat and $CO_2$ during the process of generating energy. Therefore, considering rapid decrease of fossil fuel sources and increasing global heat, alternative renewable energy sources should be made available. Renewable energy research has increased drastically in last two decades with current share of 19% towards world total energy consumption (see Figure 2.1).[1] Major renewable energy sources are wind, tidal, geothermal, and traditional biomass.[1]

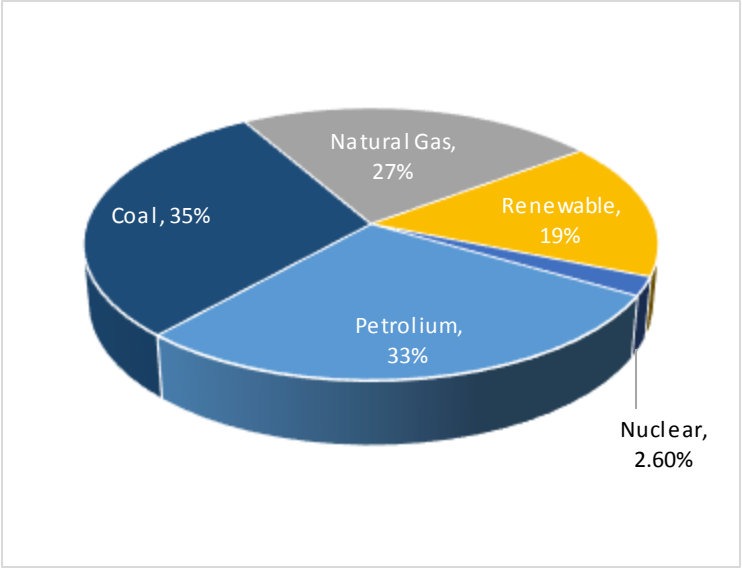


**Figure 2.1:** World Energy Consumption by Source

### 2.2 Solar Energy As-Long Term Alternative

Solar energy is an important renewable energy alternative available to mankind. The sun, an abundant source of energy, imparts 173K TW of power on earth every day.[2] Therefore, it has a huge potential to supply the world's total energy demands. However, only less than 0.1 % of world total energy consumption comes from solar photovoltaics.[1] Major obstacles for the rapid commercialization of these solar energy system are high costs of manufacturing and installations. Development of high power conversion efficiency solar cell systems with high durability can reduce these costs. Therefore, improving low cost, efficient, and durable solar cells remains one of the important goals in solar energy research.

### 2.3 Organic solar cells over inorganic solar cells

Inorganic solar cells reached a breakthrough in 1954, when the first silicon solar cell was produced by Bell labs.[3] Further development has lead silicon solar cells to reach power conversion efficiency (PCE) up to 25%.[4] Currently, most of the commercially installed photovoltaic systems are from silicon based solar cells. Research on other inorganic photovoltaic systems has also been quite successful. To date, the highest efficiency achieved from inorganic solar cells is 35%, which is based on GaInP and developed by Sharp Monolith.[4] Moreover, inorganic solar cell have excellent lifetime.

Organic photovoltaics (OPVs), on the other hand, have drawn significant interest in last two decades because of their advantages over inorganic solar cells.[5] OPVs are lightweight, cheap, and non-toxic compared to inorganic solar cells. Additionally, they are mechanically robust and flexible. Low cost fabrication on a large scale through roll-to-roll processing facilitates easy commercialization. Organic solar cells however, have

low power conversion efficiency compared to their inorganic counterparts. At present, the highest efficiency achieved for OPVs is 13.2%.[6] Stability is also an issue with OPVs, as their lifetime is currently limited to 5000 hours compared to 20 years for silicon solar cells.[5] Therefore, the most important goals in OPV research include improvement in the power conversion efficiency and stability.

### 2.4 Principle behind Organic Solar Cells

Organic solar cells, as the name implies, convert light into electricity using organic molecules. Conjugated polymers and small organic molecules are commonly used for these solar cells. Their long chain delocalization through alternate double and single bonds helps in effective electron transfer in the cell. Therefore, when light irradiates these molecules, electrons are excited and jump from bonding $\pi$ orbitals to antibonding $\pi^*$ orbitals. These orbitals are known as highest occupied molecular orbitals (HOMO) and lowest unoccupied molecular orbitals (LUMO). The energy difference between the low energy HOMO and the high energy LUMO is called the optical band gap in the semiconductor field.[7]

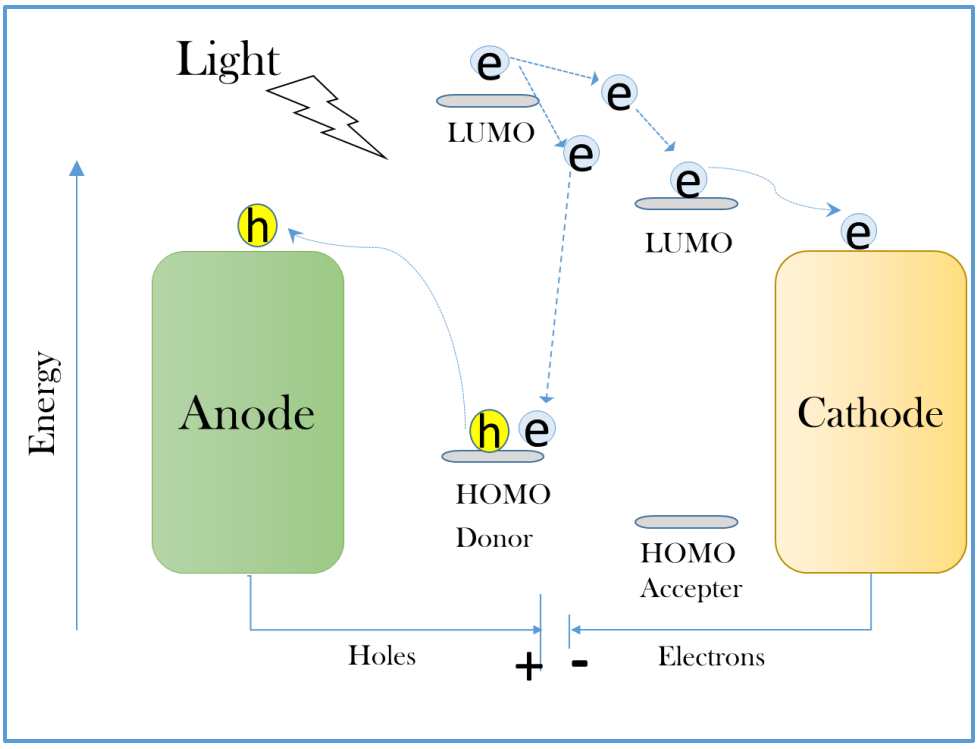


**Figure 2.2** Working of an organic solar cell in schematic form

A typical organic solar cell is comprised of p-type donor and n-type acceptor molecules. The working of a typical organic solar cell can be better understood with the help of the schematic diagram shown in Figure 2.2. First, light irradiates the p-type donor molecules. Donor molecules absorb photons and excite electrons from the HOMO energy level to the LUMO energy level. With the excitation of an electron, a vacancy that is known as "a hole" is created at the HOMO level of the donor molecule. Therefore, this step of excited electron gives an electron-hole pair known as an "exciton". This electron-hole pair separates at the interface of donor and acceptor molecules. The charge carriers now move towards their respective electrodes. Thus, electrons move towards the cathode and holes move towards the anode.

The movement of electrons and holes depends upon the work function of the electrodes. Work function is the amount of energy required to remove an electron from a

material.[8] Therefore, a lower work function material will accept an electron easily. Aluminum, which is generally used as the cathode for organic solar cells is a low work function metal. It will easily accept an electron from the LUMO level of an acceptor. On the other hand, Indium tin oxide (ITO) is a widely used high work function material in organic solar cells. It will extract holes from donor molecules easily. Thus, the extracted electrons and hole recombine with each other in the external circuit with a generation of photocurrent.

### 2.5 Different Device Architectures of Organic Solar Cell

Typical organic solar cells are made of three layers, including an active layer, an anode, and a cathode. Active layer is kept in between the anode and cathode layers. However, one of the electrode should be transparent to light. Usually, indium tin oxide used as a transparent anode layer and a metal electrode such as aluminum or calcium used as a cathode layer. There has been much research done on device architectures of organic solar cells to improve efficient charge transfer across the cell.[9]

#### 2.5.1 Single Layer Organic Solar Cell

In earlier organic photovoltaic research, the first architecture proposed was the single layer organic solar cell. In this architecture, a photoactive organic layer is sandwiched between the anode and cathode.[10] Indium tin oxide is used as a transparent hole collecting layer and aluminum or calcium as an electron collecting layer. The device architecture is shown in Figure 2.3.

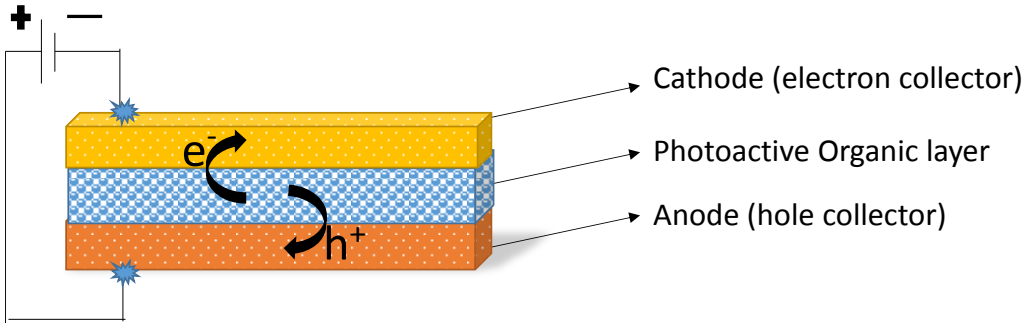


**Figure 2.3**: Schematic diagram of a single layer organic solar

In this type of device architecture, photocurrent is achieved with the help of work function difference between a metal and an electrode. This kind of device architecture limits efficient charge carrier separation.[10] Therefore, the recombination of hole and electron is prevalent in this architecture. This loss leads to low efficiency for single layer architectures. The maximum power conversion efficiency achieved with these device architectures is, 0.1%.[11]

### 2.5.2 Double Layer Organic Solar Cell

This architecture was introduced to overcome the limitation of charge recombination in single layer OPVs. Double layer organic solar cells, as the name suggests, consist of two layers sandwiched between anode and cathode (see Figure 2.4). Basically, the two layers are p-type electron donor and n-type electron acceptor. Tang, in 1986, brought this architecture, using phthalocyanines as a donor and perylene derivatives as an acceptor layer.[10] When the light strikes on donor molecules, charge carriers are generated in the donor molecules. These charge carriers separate at the interface of donor and acceptor molecules and move towards the dissimilar electrodes. The LUMO level of a donor molecule should match with the HOMO level of an acceptor

molecule to carry out this movement. The maximum power conversion efficiency achieved with this architecture was 1%.[10]

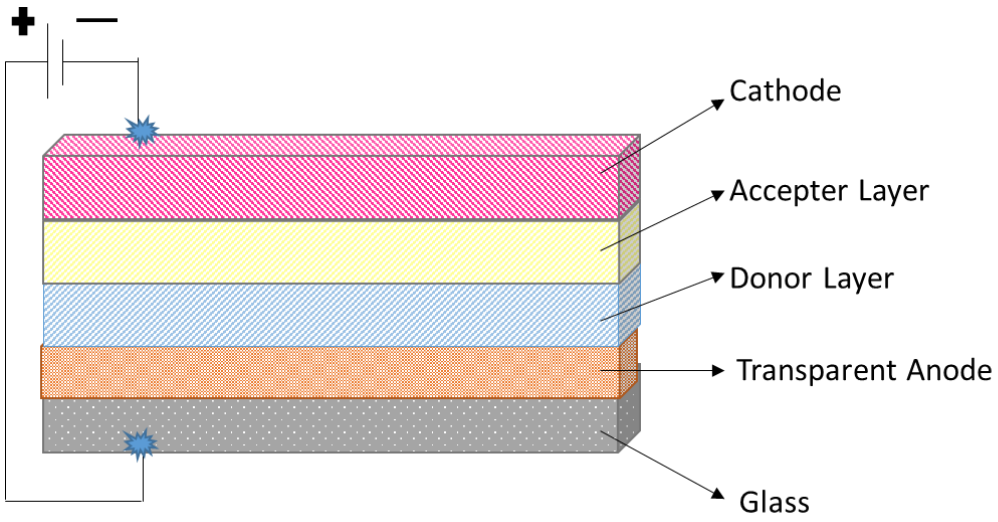


**Figure 2.4:** Two layer organic solar cell

### 2.5.3 Bulk Heterojunction (BHJ) Organic Solar Cell

This device architecture was proposed by Alan Heeger in 1995.[12] It is known as one of the breakthroughs in the field of organic solar cells. In this architecture, a blend of acceptor and donor molecules is sandwiched between an anode and a cathode layer, making a network of donor-acceptor matrix. Because of the increased interfacial area, a larger number of charge carriers is generated at the interface of donor and acceptor molecules. Therefore, with this architecture, effective charge transfer between electrodes can be achieved. Figure 2.5 shows the BHJ device architecture. Typically, conducting polymers such as poly (3-hexyl thiophene) as a donors and fullerene derivatives as acceptors are used in BHJ solar cells. Further modification in this architecture includes

inverted and tandem BHJ solar cells. Until now, this is the most efficient device architecture giving a maximum efficiency of 8.94% for a single BHJ solar cell. [13]

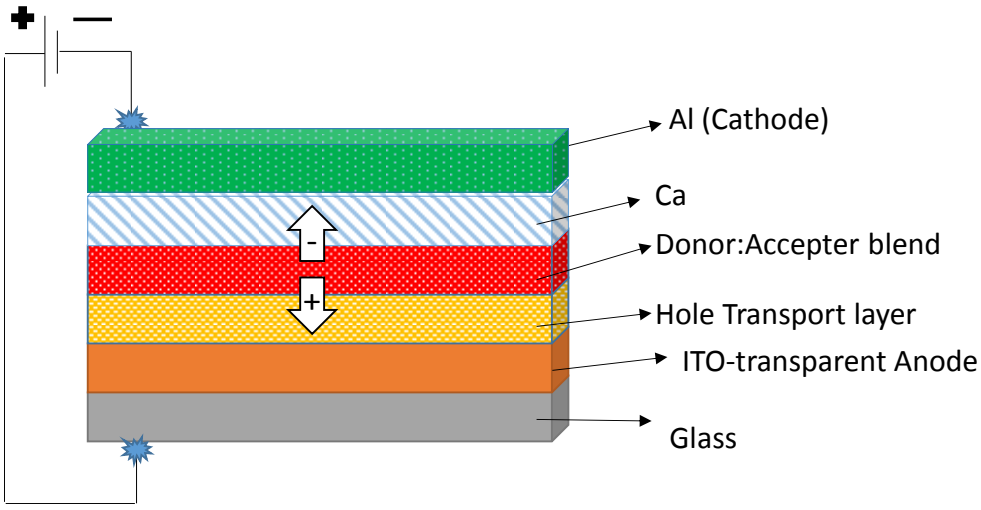


**Figure 2.5:** Bulk heterojunction organic solar cell

### 2.5.3.1 Inverted BHJ Solar Cell

One of the important concerns about BHJ solar cells is their stability and lifetime in open air.[14] The inverted BHJ solar cell is an important modification to a typical single BHJ solar cell to improve the stability and durability. In this new architecture, an inverted geometry compared to the regular BHJ cell was developed.[15] The device geometry is such that the charge carriers move in the opposite direction when compared to the single BHJ solar cell. In a regular BHJ solar cell aluminum is used as a cathode, however, being a low work function metal it oxidizes in air. Here, the high work function metal such as silver is used to extract holes while the transparent ITO electrode is used to extract electrons from the active layer. Typically, a hole blocking layer composed of Zinc oxide (ZnO) is placed in between the active layer and the transparent cathode, ITO, to hinder

the charge recombination. Figure 2.6 illustrates the device architecture of the inverted BHJ.

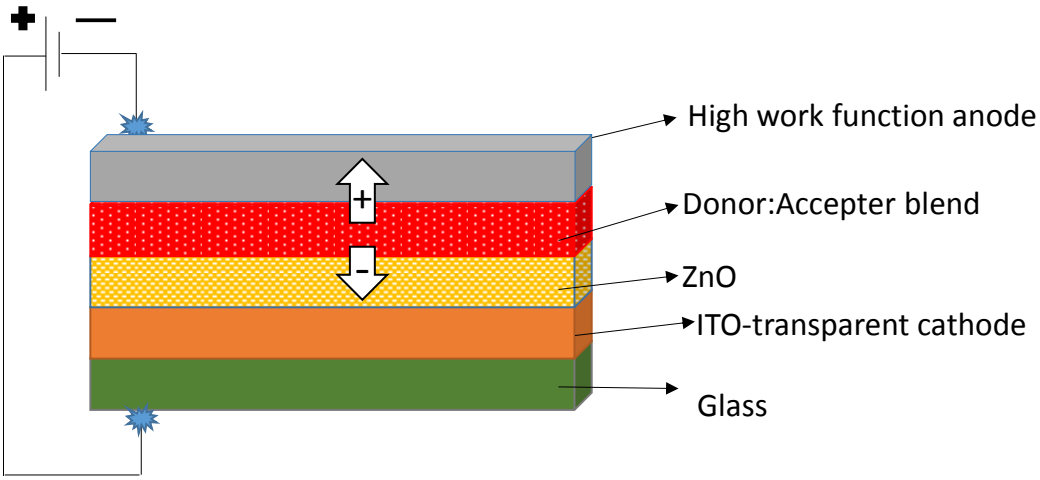


**Figure 2.6**: Inverted bulk heterojunction BHJ solar cell

### 2.5.3.2 Tandem Bulk Heterojunction Solar Cell

It has been proposed that the efficiency of regular and inverted BHJ organic solar cells is limited to a power conversion efficiency of 10%. This is mainly due to thermalization of hot charge carriers and limited light absorption.[16] Therefore, devices with the tandem configuration have drawn recent interest.[17] In this architecture, two BHJ solar cells are stacked together and interconnected by a charge transport intermediate layer. As different molecular systems can absorb different wavelength regions of the solar spectrum, tandem cells can absorb both long and short wavelength regions of the spectrum to generate electrons. With proper tuning of energy harvesting molecular systems, the overall solar spectrum can be utilized from this tandem configuration. The highest efficiency achieved with tandem configuration solar cells is close to 13%.[18]

However, there are issues in fabricating these devices such as the wetting behavior of connecting layers, use of different solvents for different layers and complex matching of band gaps.[19] Figure 2.5 shows the typical device architecture of a tandem organic solar cell. The red layer shows a red wavelength region absorbing BHJ active layer and the blue layer shows a blue wavelength region absorbing BHJ active layer. In the tandem configuration, three different cells can be stacked together, incorporating near infrared (NIR) absorbing molecules as a third layer.[20]

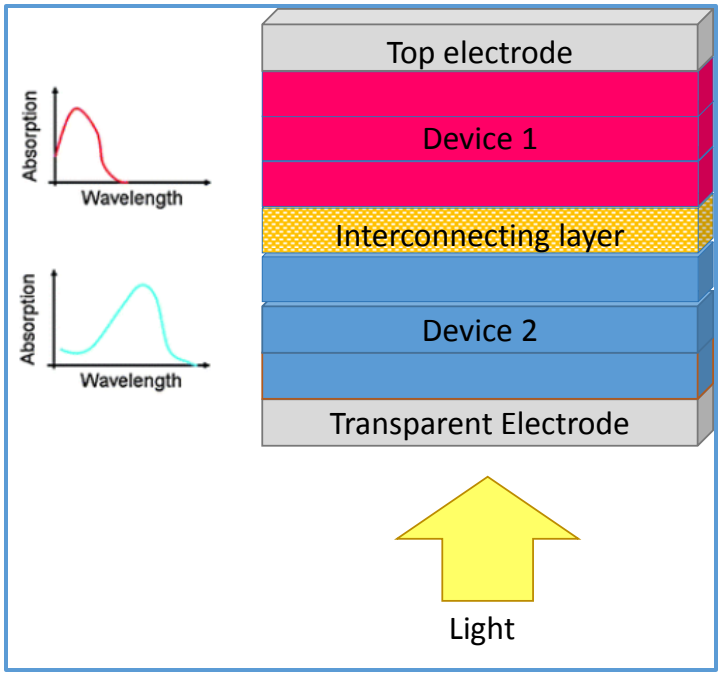


**Figure 2.7:** Tandem organic solar cell architecture

### 2.5.4 Efficiency Table of Different Device Architectures of OSC.

Table 1 summarizes the recent advancement of power conversion efficiencies achieved with different device architectures. Currently, the highest PCE record for OPVs is held by the Heliatek company.[18] They have achieved 13.2% PCE with a triple junction organic solar cell.[18]

**Table 2.1:** Efficiency Table of Different Device Architectures of OSC.

| Sr. No. | Device Architecture | References | Year | Efficiency |
|---|---|---|---|---|
| 1 | Single Layer Organic Solar Cell | Chamberlain[21] | 1950-1985 | <0.1% |
| 2 | Double Layer Organic Solar Cell | Tang[10] | 1986 | 0.95% |
| 3 | Bulk heterojunction solar cell | Shaheen et al.[22] | 2001 | 2.50% |
| 4 | Bulk heterojunction solar cell | Forrest et al.[23] | 2005 | 5.00% |
| 5 | Inverted single bulk heterojunction | Wu et al.[24] | 2012 | 9.20% |
| 6 | Double Junction Tandem Solar Cell | Yang et al.[16] | 2013 | 10.61% |
| 7 | Triple Junction Tandem Solar Cell | Heliatek[18] | 2016 | 13.20% |

### 2.5.5 Active Layer Material used for Organic Photovoltaics- Poly(3-hexylthiophene) and Fullerene C61:

Among the wide variety of organic solar cell materials, poly (3-hexylthiophene) (P3HT) and phenyl-C61 butyric acid methyl ester (PCBM) are widely used donor and acceptor materials, respectively (see Figure 2.8). This is mainly because of their low cost and easy solution processing. Moreover, P3HT:PCBM active layer morphology can be manipulated using various methods such as solvent annealing, thermal annealing, change in donor:acceptor ratio and varying the solvent type for device processing. P3HT is a semiconducting polymer having alternative single and double bonds that effectively delocalize $\pi$ electrons of each aromatic ring. PCBM is a spherical fullerene-based carbon molecule that can act as an acceptor. The Power conversion efficiencies (PCEs) achieved with this donor-acceptor system vary depending upon the fabrication methodologies and device structures. The PCEs obtained with these molecules are in the range of 3-5%.[25-26] Recently, a PCE of 8.4% was obtained by the Heliatek Company using P3HT and a fullerene derivative.[27]

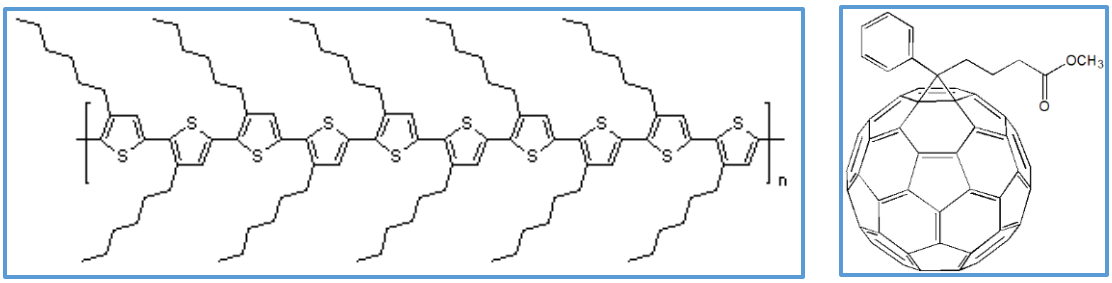


**Figure 2.8:** Chemical structures of P3HT (left) and PCBM (right)

These materials have also been employed in the form of nanoparticles in BHJ solar cells. Employment of nanoparticles as a BHJ layer drastically improves the charge transport. It was evidenced by electrical and structural characterization that it creates continuous pathways for electrons and holes throughout the nanostructures.[28] Size and ratio of nanoparticles in the BHJ layer effect the packing of nanoparticles, which is inherently related to charge transport. Therefore the photovoltaic performance of BHJ solar cells can be improved by controlling the size and ratio of nanoparticles.[29] Additionally, use of chlorinated solvents can be avoided, as these nanoparticles are easily suspended in aqueous media, and device fabrication can be performed as an ink-based, water processible suspension. Recently, Venkatraman et al. have developed self-assembled P3HT-PCBM nanoparticles and incorporated them in a BHJ solar cell assembly.[28] The efficiency achieved with this system was about 2%. However, simulation studies indicate that higher efficiency can be achieved with proper control of interconnection layers and thickness.

## 2.6 Various Electrode Materials used for BHJ Organic Solar Cell

Various materials are used as anodes or cathodes for BHJ solar cells. As discussed earlier, the cathode collect electrons and anode collect holes. Therefore, selection of these

electrodes depends upon the work function. Most common materials for anodes are high work function metal oxides, for example, indium tin oxide, and noble metals such as gold and platinum. Similarly, commonly used cathode materials are low work function metals such as aluminum, calcium, magnesium and copper. The work function of an anode or cathode can be modified using a buffer layer. A low work function buffer layer is used to modify the cathode. Typically, these buffer layers are low or high work function metal oxides. Examples of low work function metal oxides are titanium oxide and zinc oxide, which are used as cathode buffer layers. Similarly, anodes can be modified using high work function molybdenum oxide and nickel oxide. Table 2.2 gives the work function values of different materials used in BHJ solar cells.

**Table 2.2:** Work function values of various metals and metal oxides used in organic solar cells.[8,30–32]

| Metal | Work Function (eV) | Metal Oxide | Work Function (eV) |
|---|---|---|---|
| Gold | 5.1-5.47 | $TiO_2$ | 5.34 |
| Platinum | 5.12-5.93 | ZnO | 5.71 |
| Aluminum | 4.06-4.26 | $Ta_2O_5$ | 4.19 |
| Calcium | 2.87 | $ZrO_2$ | 3.82 |
| Magnesium | 3.66 | $MoO_3$ | 6.81 |
| Copper | 4.53-5.10 | NiO | 4.33 |
| Silver | 4.67-4.81 | CuO | 5.20 |
| Titanium | 4.30 | $WO_2$ | 7.00 |

## 2.7 Improvement of morphology using solvent annealing and thermal annealing

### 2.7.1 Solvent Annealing

Solvent annealing is a process in which the photoactive organic layer is kept in a high concentration solvent environment. It was observed that solvent annealing can be

used as a treatment to control the morphology of the active layer film.[33] Verplogen, et al. studied solvent annealing of an active layer using different solvents.[34] This study has shown that solvent annealing results in smaller phase segregation domains in the active layer. These small domains are important in the BHJ structure because they improve the interfacial area and facilitate charge carriers to reach their respective electrodes. Important parameters in the solvent annealing include solvent annealing time and type of solvent.[35,36]

Solvent annealing causes the polymer layer to swell, which further leads to reduction in the π-π stacking distance and improves crystalline order of the donor polymer layer. Crystallization due to solvent annealing causes the development of the interpenetrating network of donor-acceptor layers. This network usually diffuses through adjacent cathode layers, and provides percolated pathways to the charge carriers. This improved charge transfer mechanism results in increased power conversion efficiency. With this technique, the maximum efficiency achieved is 4.4%.[37]

### 2.7.2 Thermal Annealing

In thermal annealing, devices are placed at a certain temperature for a certain period of time. Thermal annealing, similar to solvent annealing, has been proven to improve the morphology of the polymer-fullerene blend.[38] It can be done in two ways; pre- or post- annealing. As the diffusion lengths of charge carriers are limited to 3 to 30 nm,[39] thermal annealing helps to increase the domain sizes of a blend. These domain sizes can be controlled with the annealing temperature and time. Padinger, et al., in 2003, optimized the annealing temperature to 75 °C with the optimized annealing time of 5-6 minutes.[40] Li et al. studied the film morphology using AFM after annealing treatment at

different temperatures.[41] They found that surface roughness of the film increases above the glass transition temperature. The optimum annealing temperature reported by this work was 70 -110 °C.[41] Furthermore, TEM studies performed by Schlenkar et al. confirmed the interpenetrating network of the donor-acceptor blend.[42] However, the power conversion efficiency for thermally annealed devices has been limited to 5.4%. Therefore, these techniques need to be developed further to improve the morphology of the film and thus, gain higher efficiency.

### 2.8 Photovoltaic Characteristics of a solar cell

The photovoltaic characteristics of a solar cell can be studied with a J-V plot which is obtained from measuring current (I) with respect to the bias voltage (V). The photovoltaic parameters of a solar cell are fill factor (FF), open circuit voltage ($V_{oc}$), short circuit current density ($J_{sc}$) and power conversion efficiency (PCE). Figure 2.9 shows these parameters and an example of a J-V curve.

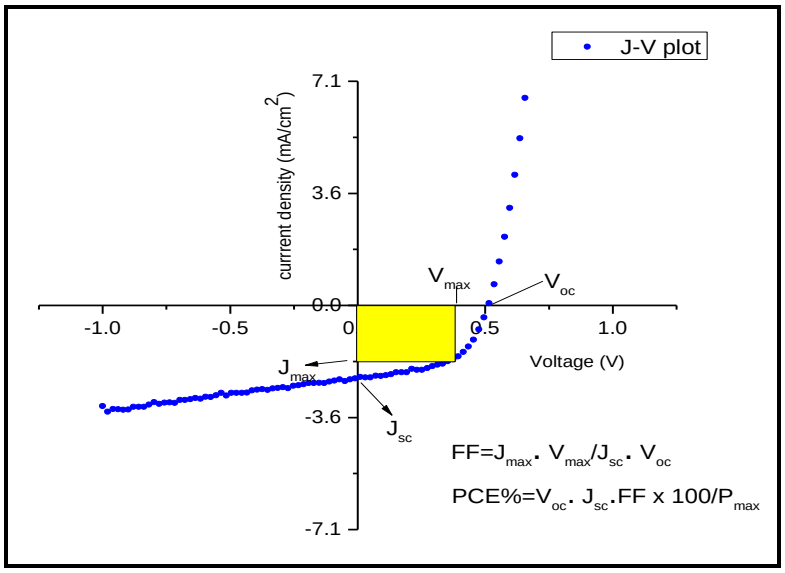


**Figure 2.9:** Photovoltaic characteristics of a solar cell

### 2.8.1 Short Circuit Current Density ($J_{sc}$)

Short circuit current density ($J_{sc}$) is the maximum current per unit area obtained from a cell when subjected to a short circuit connection. Therefore, it is the current value obtained per unit area at zero voltage. $J_{sc}$ attributes to the efficiency of a solar cell due to light generated charge carriers. It depends on many factors such as the area of the cell, light intensity, spectrum of the incident light, and collection probability by the electrodes.

### 2.8.2 Open circuit voltage ($V_{oc}$)

The voltage output obtained through the circuit at zero current value is the open circuit voltage ($V_{oc}$). It depends upon the saturation current and current generated through radiation. It is directly associated with the band gap of the donor and acceptor molecules. Usually, the difference in energy level of the LUMO of a donor and the LUMO of an acceptor gives $V_{oc}$ for a particular blend. It has been observed that the value of $V_{oc}$ is directly proportional to change in band gap of donor and acceptor materials.[43]

### 2.8.3 Fill factor (FF)

Fill factor (FF) is the ratio of maximum power from the solar cell to the product of a short circuit current ($I_{sc}$) and an open circuit voltage ($V_{oc}$). This means that it determines the maximum power from the circuit in conjunction with the $I_{sc}$ and $V_{oc}$. In an I-V graph, it is measures from maximum square area which can fit in the IV curve as shown in the yellow shaded area of the Figure 2.7. The magnitude of the square indicates higher power output.[43]

### 2.8.4 Power Conversion Efficiency (PCE)

PCE is the most important parameter of a solar cell that measures the quality and performance of the cell. It can be defined as the ratio of power output from the cell to the

power input. In other words, PCE is the ratio between the electrical energy achieved from the solar cell to light energy irradiated on the cell.[43] The efficiency comparison between two different solar cells is based on the calibrated measurements performed under standard condition such as AM 1.5 and 1 sun intensity of light. The power input for PCE calculation is taken as 100 mW/cm$^2$ for 1 sun. Further, spectral mismatch should be avoided for accurate measurement of PCE. Basically, the lamp used for photovoltaic study should have the same emission spectrum as that of the sun.[44]

PCE can be calculated by following formula:

$$Pmax = V_{OC}.I_{SC}\ .FF$$

$$PCE(\%) = \frac{V_{OC}.I_{SC}\ .FF}{P_{input}} \times 100$$

### 2.9 Challenges

#### 2.9.1 Power Conversion Efficiencies

In terms of power conversion efficiency, OPVs lag behind compared to commercial silicon solar cells, which have already reached PCE of 24%.[5] Therefore, further improvement in power conversion efficiency remains the main goal for this research. Main reasons behind low efficiency of organic solar cells include, charge carrier imbalance, difficulty in controlling morphology of an active layer, and limited photon absorption.[42]

**a) Morphology control**: Morphology control is crucial in OSCs to obtain high efficiency solar cells. Although efficiency values have increased in recent years, most of them have been achieved through trial and error, morphology control is still a challenge

in OSCs. In an OSC, when light strikes on active material, it creates excitons. These excitons have short diffusion lengths. Therefore, it is necessary to form an ordered structure of an active layer, to facilitate an easy transport of charge carriers. Charge carriers need percolated pathways to reach the oppositely charged electrodes and controlled morphology can improve these pathways.

**i) Solvent and Thermal Annealing**:

Charge transport studies showed that solvent and thermal annealing improves the electron hole mobility across the two electrodes. Padinger et al. in 2003, noticed that solvent and thermal annealing significantly improves the morphology of the active layer. They observed improvement in efficiency for annealed devices to 3.5% over non-annealed ones at 2.5%. [25]

**ii) Choice of Solvent:**

Hoppe et al. studied the effect of solvent on performance of solar cell.[45] They compared the device performances for P3HT:PCBM based system using different solvents. They have found chlorobenzene gives good morphology because of excellent solubility of P3HT and PCBM materials in chlorobenzene. Further solvent annealing with chlorobenzene improved the crystallinity in the active layer.[46]

**iii) Inclusion of Additives:**

Studies on P3HT: PCBM devices have shown that inclusion of surfactants in the active layer significantly improves the conductivity in the structure. Peet et al. introduced alkyl thiols in the casting solution of an active layer. Because of improved ordered structure device performance was improved by a significant 30%.[39]

**iv) Regioregularity**

Li et al. studied the effect of regioregularity of P3HT donor polymer on device performance. Their studies showed that regioregular P3HT polymer forms a lamellar packing in the active layer. This packing results in an ordered structure of the donor-acceptor layer.[47]

**v) Ratio of donor and acceptor materials**

Numerous studies have been done on effects of donor:acceptor ratio on active layer morphology. Phase diagram show improved morphology and increased efficiency for P3HT:PCBM solar cells at 1:1 ratio, studied by Muller et al.[47]

**b) Photon absorption:** Compared to inorganic solar cells light absorption bands for organic solar cells are narrow. Most of the polymers and organic molecules do not absorb across the full solar spectrum. The most widely used donor polymer, P3HT, absorbs only the red wavelength region of solar spectrum.[48] This implies that, not all the incident light on an OSC converts light into photocurrent. This counts to optical losses and one of the challenges to get higher power conversion efficiency. It is noticed that low band gap materials absorb a larger spectrum of light. For example, material with a band gap of 1.1 eV absorbs approximately 78% of a solar spectrum.[49] Therefore researchers have been working on development of novel narrow band gap materials.

Ideally, an incident photon should have an energy equivalent to the energy difference between the HOMO and LUMO of the materials. However, when higher or lower energy photons fall on donor materials, a bound electron and hole with opposite spin are created. The coulombic attraction between these charge carriers is higher than

the work function difference between donor and acceptor molecules. Therefore, these charge carriers do not participate in band-to-band transition localization in the molecule itself. This results in loss of photocurrent in the cell.

In addition to development of low band gap materials, researchers have worked with adjusting the donor and acceptor ratio to improve the light absorption. Cates et al. found increased light absorption at a donor-acceptor ratio of 1:1, with higher efficiency of 2.51% compared to 1.94% for a 1:4 donor-acceptor ratio.[47]

As discussed earlier, the energy difference between the HOMO of a donor material and the LUMO of an acceptor should be small. This reduces the work function between donor and acceptor materials and facilitates easy charge transfer, and importantly, enhances light absorption. Zhang et al. developed AFCO-green-9, a donor polymer with low LUMO energy level to align with the energy level of acceptor molecules.[46] They have obtained 2.3% efficiency with a regular BHJ solar cell, and AFCO-green-9 seems promising as a material for energy alignment in tandem solar cells. Qiaoshi et al. synthesized low bad gap materials to align with the energy levels of P3HT:PCBM system.[50] They found that doping low band gap materials with the P3HT:PCBM system has improved the efficiency from 3.05% to 3.72%.

Tandem device architecture significantly resolved the problem of photon loss. In tandem architecture, two or more devices are stacked together to absorb complementary sections of the spectrum. These cells are connected together with an intermediate charge transport layer which provides sites for recombination to electrons and holes. Hadipour et al. found 2.5 times improved efficiency for tandem solar cells compared to single BHJ solar cells.[49] Because low band gap materials cannot significantly contribute to higher

cell performance, large and narrow band gap materials are incorporated together. Heliatek, a German based company, employed near infrared (NIR) absorbing material in a tandem architecture cell and achieved 13.2% efficiency recently.[18] Major limitations of tandem solar cells are complex fabrication process and difficulty in band gap matching of individual layer of materials.

Increased active layer thickness significantly improves the light absorption because of the presence of more material. However, thickness is limited to 100-200 nanometers because of the short diffusion lengths of excitons. Li et al. studied the effect of active layer thickness on power conversion efficiency.[41] They found the optimum thickness for P3HT:PCBM layer at 63 nm with efficiency of 4%.

**c) Charge carrier imbalance**

Charge carrier imbalance is a naturally occurring phenomenon with disordered morphology. As the exciton diffuses through the interface between donor and acceptor, it separates and moves as a charge carrier towards the oppositely charge electrode. However, due to absence of channels or percolated pathways for charge carriers, they get lost or recombined. It generates excess space charge in the donor-acceptor layer and reduces the performance of BHJ cells. Usually, hole mobility across the electrodes is less than electron mobility; however, it was noticed that blending of PCBM with P3HT helped in balancing charge transport.[51] It was also observed that solvent annealing and thermal annealing techniques drastically improves the hole mobility across the active layer. Improvement in crystallization during the annealing process is associated with an increase in hole mobility.

### 2.9.2 Stability

Ideally, solar cell performance should not drop over a period of time and it should depend a little on weather conditions such as hot/cold and dry/humid. OPVs lags far behind in stability when compared to their commercial counterpart, silicon solar cells. Therefore, this is one of the biggest obstacles to making OPVs a commercial competitor. There are two types of stability concerns for OPVs; 1) Material stability, and 2) Physical stability. Material stability includes stability of the active layer, metal electrodes, and electron/hole transport layers. Physical stability is related to mechanical robustness, weariness, and abrasion of these devices.

Encapsulation of OPVs has improved physical stability of OPVs to a large extent. Postcavage et al. showed that encapsulation of BHJ solar cells with aluminum oxides significantly improves the durability.[52] However, material stability is still an important concern for OPVs.[53] The degradation of the material in organic solar cells occurs mainly due to two reasons; first, illumination of organic matter leads to number of photolytic and photochemical reactions, this degrades organic matter. Second, atmospheric components such as water and oxygen react with metal electrodes/organic materials, and this results in the hampering of photovoltaic performance of solar cells. Amongst all materials incorporated in BHJ solar cells, the active layer is most prone to degradation and this directly affects the photovoltaic performance of a cell. Photodegradation studies of P3HT:PCBM active layers show that, oxygen reacts fairly rapid with these materials.[54] The oxidized materials form traps for electron transport within the blend. In conclusion, effective charge transfer is hampered in BHJs due to an oxidizing environment.[14]

Metal electrode degradation is attributed to atmospheric molecular oxygen and water. This process goes by two mechanisms. First, it forms an oxide which is an insulator. Therefore, it affects the photovoltaic performance of a cell by forming a charge transport barrier. Second, the microporous metal electrode will provide channels to molecular oxygen and water, which further help in photo-oxidation of an active layer. Hermenau et al. noticed that water degrades the OPVs more rapidly than molecular oxygen.[55]

With the improvements in materials and processing techniques, device stability of OPVs has been increasing with a steady pace in the last decade. Devices made in late 90's have life times limited to a few hours. However, with the continuous research work, stability has been improved significantly. An important breakthrough in improvement of stability was made by Shaheen et al. in 2007 when they made an inverted architecture BHJ.[15] The inverted architecture helped in reducing the exposure of active layer and metal electrode to the atmospheric oxygen and water. In this device architecture, they used a high work function silver electrode as the anode. Inverted architecture has been also applied to the tandem configuration by You et al. in 2013. Recently, Heliatek developed a BHJ solar cell with lifetime of 10,000 hours.[9]

### 2.10 Solar Cell Fabrication Methods

There are unsolved problems for large-scale fabrication of organic solar cells. These included material cost and the complexity of fabrication processing.[56] In the field of commercial photovoltaics, there are various techniques available for large scale manufacturing. These techniques are divided sharply into two parts - printing and coating.

Printing provides more sharp, accurate and complex shape to a pattern; while coating gives uniform layer but less shape accuracy. Roll-to-roll printing is the most efficient and widely used fabrication technique.[57] This technique is material dependent and some of the important parameters to be considered for its use are viscosity of the material, surface tension, temperature stability, drying time, and minimum achievable thickness. Different printing and coating techniques are explained as follows:

### 2.10.1 Casting

This is the simplest coating method available for fabrication of organic solar cells. In this method, solution is placed on a horizontal substrate and allowed to dry. However, this method lacks in control of the thickness and sometimes picture framing effects can be observed on the film.

### 2.10.2 Spin Coating

It is the best method available for lab scale development of organic solar cells. In this method, solution is dispensed on the substrate and then subjected to high spin rate. Spinning helps the solution to spread uniformly on the substrate, which simultaneously dries due to the centrifugal force. The film thickness can be easily monitored depending on the spin rate or angular velocity.[58] Spin rate of the spin coater is inversely proportional to the thickness of the film. This technique provides reproducible and homogenous films in spite of complexity in the film formation. The maximum area coated with this technique is limited to 30 $cm^2$.[57] This method has been practiced in the microelectronic industry for many years for the fabrication of transistors, compact discs (CDs), and digital versatile discs (DVDs).

### 2.10.3 Spray Coating

This is an alternative technique that has been proven to have low cost for high surface area substrates. Although the most common and convenient method for lab scale work is spin coating, because of its limitation to coat small areas, different techniques like spray coating are studied. It is a traditional spray coating method in which solution is dispensed on the substrate using air flow or jet stream.[59] Spray coating method is divided into two types 1) Air brush spray coating, and 2) Ultrasonic spray coating.

#### 2.10.3.1 Air Brush Spray Coating

An air brush is generally used for the deposition of a uniform thin film with a spray of small droplets on the surface. An air-gun is used to form a spray of material and a jet flow via inert gasses. In this technique, more passes across the substrate can make a uniform film over a large area. Film homogeneity and thickness depends upon the number of passes and jet flow velocity.[58]

#### 2.10.3.2 Ultrasonic Spray Coating

Ultrasonic spray coating is another way of dispensing solution in a spray form for deposition of materials in OPVs. In this system, ultrasonic transducers are attached to the dispensing unit that causes an ultrasonication effect at the nozzle. Due to this, extremely small droplets dispense through the nozzle at very low velocity. Compared to air-brush technique, this method is better because the velocity of the dispensed droplets is considerably less. Because of the low velocity, droplets do not repel back from the surface, giving a homogenous deposition layer. The frequencies available for ultrasonication are 35 kHz, 40 kHz or 60 kHz and the frequency selection depends upon the solution deposited and the surface coated.[59] Generally, this system is suitable for roll-

to-roll processing as larger areas can be coated. In roll-to-roll processing, the ultrasonic spray system is attached to the stepper motor which can move back and forth for multiple passes during deposition. Advantages of ultrasonic spray include rapid transfer efficiency of the solution, anti-clogging for semisolid solutions, longevity, uniform droplet size deposition, homogenous film formation and spray without air flow.

**Working of an ultrasonic spray coating**

In the ultrasonic spray coating method, the depositing liquid is transferred to the tip of the ultrasonic spray nozzle, which is connected to the ultrasonic transducers. These transducers are connected to the control system and spray coating parameters can be handled through the controller. Some of the major parameters include flow rate, jet force, conveyer, nozzle power, and spray width. The liquid to be deposited is filled in the syringe connected to the syringe dispenser unit with a set flow rate. The liquid passes through the tubing from the syringe to the ultrasonic nozzle. When the liquid reaches the nozzle, the ultrasonic transducers produces extremely small sized droplets. The number of passes can be controlled with the moving step stage. This step ensures that the substrate gets deposited multiple times forming a homogenous layer.[6]

### 2.10.4 Screen Printing

This technique is one of the oldest methods being used to dye textiles. However, it has significant applications in the electronics especially in OPV fabrication, as control of the shape of the printing layer is very important. Screen printing facilitates printing complex shapes with high accuracy. In this technique, a mesh is used through which ink or paste is applied on the substrates with a blocking stencil. A blade with the ink is

moved in one direction to print and the substrate gets printed depending upon the blocking stencil. Its advantages include ease of processing and accuracy.[57]

### 2.10.5 Intense Pulse Light (IPL) Sintering

Various post fabrication techniques are required to achieve a final functional solar cell for the solution processed OPV fabrication. Some of these major techniques include annealing, curing, drying, and sintering.[60] Sometimes, integrated methods are used, including more than two of the methods mentioned above. For metal nanoparticale or nanoinks, a sintering process is involved improving the efficiency of the layer in terms of conductivity. Sintering can be done by microwave, plasma, heat, or intense pulse light (IPL) methods. Heat sintering requires high temperatures that may cause degradation of organic layers in the OPVs. On the contrary, IPL treatment enables easy sintering of the metal layer without affecting the stability of the organic layers. This nondestructive technique takes a fraction of a second to perform. Its limitations include high intensity ultraviolet light, which may affect the organic layers.[61]

## References


(1) Foley, T.; Thornton, K.; Hinrichs-rahlwes, R.; Sawyer, S.; Sander, M.; Taylor, R.; Teske, S.; Lehmann, H.; Alers, M.; Hales, D. <*REN12-GSR2015_Onlinebook_low1.pdf*>; 2015.

(2) Koidis, C.; Logothetidis, S.; Ioakeimidis, A.; Laskarakis, A.; Kapnopoulos, C. Key factors to improve the efficiency of roll-to-roll printed organic photovoltaics. *Org. Electron. physics, Mater. Appl.* **2013**, *14* (7), 1744–1748.

(3) Blandford, R.; Watkins, M. This Month in Physics History: April 25, 1954: Bell Labs Demonstrates the First Practical Silicon Solar Cell. *APS News* **2009**.

(4) Green Martin, Emery Keith, Hishikawa Yoshihiro, Warta Wilhelm, D. D. Solar Cells Utilizing Small Molecular Weight Organic Semiconductors. *Prog. Photovolt Res. Appl.* **2015**, *15*, 659–676.

(5) Xiao, S.; Xu, S. High-Efficiency Silicon Solar Cells—Materials and Devices Physics. *Crit. Rev. Solid State Mater. Sci.* **2014**, *39* (4), 277–317.

(6) Vilkman, M.; Hassinen, T.; Kerunen, M.; Pretot, R.; Van Der Schaaf, P.; Ruotsalainen, T.; Sandberg, H. G. O. Fully roll-to-roll processed organic top gate transistors using a printable etchant for bottom electrode patterning. *Org. Electron. physics, Mater. Appl.* **2015**, *20* (February), 8–14.

(7) Heeger, A. J. 25th anniversary article: Bulk heterojunction solar cells: Understanding the mechanism of operation. *Adv. Mater.* **2014**, *26*, 10–28.

(8) Brabec, C. J.; Cravino, a.; Meissner, D.; Sariciftci, N. S.; Rispens, M. T.; Sanchez, L.; Hummelen, J. C.; Fromherz, T. The influence of materials work function on the open circuit voltage of plastic solar cells. *Thin Solid Films* **2002**, *403-404*, 368–372.

(9) Ragoussi, M.-E.; Torres, T. New generation solar cells: concepts, trends and perspectives. *Chem. Commun.* **2015.**

(10) Tang, C. W. Two-layer organic photovoltaic cell. *Appl. Phys. Lett.* **1986**, *48*, 183–185.

(11) Kampas, Frank and Gouterman, M. Photovoltaic Properties of octaethylporphyrin and tetraethylporphyrin. *J. Phys. Chem.* **1977**, *81*, 690–695.

(12) Yu, G.; Gao, J.; Hummelen, J. C.; Wudl, F.; Heeger, a. J. Polymer Photovoltaic Cells: Enhanced Efficiencies via a Network of Internal Donor-Acceptor Heterojunctions. *Science (80-. ).* **1995**, *270*, 1789–1791.

(13) Welch, G. C.; Perez, L. A.; Hoven, C. V; Zhang, Y.; Dang, X.-D.; Sharenko, A.; Toney, M. F.; Kramer, E. J.; Nguyen, T.-Q.; Bazan, G. C. A modular molecular framework for utility in small-molecule solution-processed organic photovoltaic devices. *J. Mater. Chem.* **2011**, *21* (34), 12700–12709.

(14) Jurgensen, M.; Norrman, K.; Gevorgyan, S. a.; Tromholt, T.; Andreasen, B.; Krebs, F. C. Stability of polymer solar cells. *Adv. Mater.* **2012**, *24* (5), 580–612.

(15) Shaheen, S. Inverted bulk-heterojunction plastic solar cells. *SPIE Newsroom* **2007**, 2–4.

(16) You, J.; Dou, L.; Yoshimura, K.; Kato, T.; Ohya, K.; Moriarty, T.; Emery, K.; Chen, C.-C.; Gao, J.; Li, G.; et al. A polymer tandem solar cell with 10.6% power conversion efficiency. *Nat. Commun.* **2013**, *4*, 1446.

(17) Odobel, F.; Le Pleux, L.; Pellegrin, Y.; Blart, E. New photovoltaic devices based on the sensitization of p-type semiconductors: Challenges and opportunities. *Acc. Chem. Res.* **2010**, *43* (8), 1063–1071.

(18) Heliatek. No Title http://www.heliatek.com/en/press/press-releases/de.

(19) Albrecht, S.; Yilmaz, S.; Dumsch, I.; Allard, S.; Scherf, U.; Beaupré, S.; Leclerc, M.; Neher, D. Solution Processed Organic Tandem Solar Cells. *Energy Procedia* **2012**, *31*, 159–166.

(20) Chen, C.-C.; Dou, L.; Gao, J.; Chang, W.-H.; Li, G.; Yang, Y. High-performance semi-transparent polymer solar cells possessing tandem structures. *Energy Environ. Sci.* **2013**, *6* (9), 2714–2720 .

(21) Chamberlain, G. a. Organic solar cells: A review. *Sol. Cells* **1983**, *8* (1), 47–83.

(22) Shaheen, S. E.; Brabec, C. J.; Sariciftci, N. S.; Padinger, F.; Fromherz, T.; Hummelen, J. C. 2.5% efficient organic plastic solar cells. *Appl. Phys. Lett.* **2001**, *78* (6).

(23) Xue, J.; Rand, B. P.; Uchida, S.; Forrest, S. R. Mixed donor-acceptor molecular heterojunctions for photovoltaic applications. II. Device performance. *J. Appl. Phys.* **2005**, *98* (12), 1–14.

(24) He, Z.; Zhong, C.; Su, S.; Xu, M.; Wu, H.; Cao, Y. Enhanced power-conversion efficiency in polymer solar cells using an inverted device structure. *Nat. Photonics* **2012**, *6* (9), 593–597.

(25) Padinger, F.; Padinger, F.; Rittberger, R. S.; Rittberger, R. S.; Sariciftci, N. S.; Sariciftci, N. S. Effects of postproduction treatment om plastic solar cells. *Adv. Funct. Mater.* **2003**, *13* (1), 85.

(26) Chirvase, D.; Parisi, J.; Hummelen, J. C.; Dyakonov, V. Influence of nanomorphology on the photovoltaic action of polymer–fullerene composites. *Nanotechnology* **2004**, *15*, 1317–1323.

(27) Zhong, Y.; Trinh, M. T.; Chen, R.; Purdum, G. E.; Khlyabich, P. P.; Sezen, M.; Oh, S.; Zhu, H.; Fowler, B.; Zhang, B.; et al. Molecular helices as electron acceptors in high-performance bulk heterojunction solar cells. *Nat Commun* **2015**, *6*.

(28) Han, X.; Bag, M.; Gehan, T. S.; Venkataraman, D.; Maroudas, D. Analysis of Charge Transport and Device Performance in Organic Photovoltaic Devices with Active Layers of Self-Assembled Nanospheres. *J. Phys. Chem. C* **2015**, acs.jpcc.5b09421.

(29) Yamamoto, N. a. D.; Payne, M. E.; Koehler, M.; Facchetti, A.; Roman, L. S.; Arias, A. C. Charge transport model for photovoltaic devices based on printed polymer: Fullerene nanoparticles. *Sol. Energy Mater. Sol. Cells* **2015**, *141*, 171–177.

(30) Bivour, M.; Temmler, J.; Steinkemper, H.; Hermle, M. Molybdenum and tungsten oxide: High work function wide band gap contact materials for hole selective contacts of silicon solar cells. *Sol. Energy Mater. Sol. Cells* **2015**, *142*, 34–41.

(31) Mahlman, G. W. Work functions and conductivity of oxide-coated cathodes. *J. Appl. Phys.* **1949**, *20* (2), 197–202.

(32) Greiner, M. T.; Chai, L.; Helander, M. G.; Tang, W. M.; Lu, Z. H. Metal/metal-oxide interfaces: How metal contacts affect the work function and band structure of MoO3. *Adv. Funct. Mater.* **2013**, *23* (2), 215–226.

(33) Campoy-Quiles, M.; Ferenczi, T.; Agostinelli, T.; Etchegoin, P. G.; Kim, Y.; Anthopoulos, T. D.; Stavrinou, P. N.; Bradley, D. D. C.; Nelson, J. Morphology evolution via self-organization and lateral and vertical diffusion in polymer:fullerene solar cell blends. *Nat. Mater.* **2008**, *7* (February), 158–164.

(34) Verploegen, E.; Miller, C. E.; Schmidt, K.; Bao, Z.; Toney, M. F. Manipulating the Morphology of P3HT–PCBM Bulk Heterojunction Blends with Solvent Vapor Annealing. *Chem. Mater.* **2012**, *24* (20), 3923–3931.

(35) Li, G.; Shrotriya, V.; Yao, Y.; Huang, J.; Yang, Y. Manipulating regioregular poly(3-hexylthiophene) : [6,6]-phenyl-C61-butyric acid methyl ester blends—route towards high efficiency polymer solar cells. *J. Mater. Chem.* **2007**, *17*, 3126.

(36) István Z. Kiss; Géza Mándi; and Mihály T. Beck, Artificial Neural Network Approach to Predict the Solubility of C60 in Various Solvents. *J. Phys. Chem. A* **2000**, *104* (34), 8081–8088.

(37) Li, G.; Shrotriya, V.; Huang, J.; Yao, Y.; Moriarty, T.; Emery, K.; Yang, Y. High-efficiency solution processable polymer photovoltaic cells by self-organization of polymer blends. *Nat Mater* **2005**, *4* (11), 864–868.

(38) Kim, J.; Lee, J.; Han, C.; Lee, N.; Chung, I.-J. Effect of thermal annealing on the lifetime of polymer light-emitting diodes . *Appl. Phys. Lett.* , 2003, *82* , 4238–4240.

(39) Peet, J.; Kim, J. Y.; Coates, N. E.; Ma, W. L.; Moses, D.; Heeger, a J.; Bazan, G. C. Efficiency enhancement in low-bandgap polymer solar cells by processing with alkane dithiols. *Nat. Mater.* **2007**, *6*, 497–500.

(40) Padinger, F.; Rittberger, R. S.; Sariciftci, N. Effects of postproduction treatment on plastic solar cells . *Adv. Funct. Mater.* , 2003, *13* , 85–88.

(41) Li, G.; Shrotriya, V.; Yao, Y.; Yang, Y. Investigation of annealing effects and film thickness dependence of polymer solar cells based on poly(3-hexylthiophene). *J. Appl. Phys.* **2005**, *98*, 1–5.

(42) Schlenker, C. W.; Thompson, M. E. The molecular nature of photovoltage losses in organic solar cells. *Chem. Commun. (Camb).* **2011**, *47* (13), 3702–3716.

(43) Yang, Y.; Li, G. *Progress in High- Efficient Solution Process Organic Photovoltaic Devices*; 2015.

(44) Emery, K.; Moriarty, T. Accurate measurement of organic solar cell efficiency. *Spie* **2008**, *7052* (1), 70520D – 70520D – 6.

(45) Maennig, B.; Drechsel, J.; Gebeyehu, D.; Simon, P.; Kozlowski, F.; Werner, a.; Li, F.; Grundmann, S.; Sonntag, S.; Koch, M.; et al. Organic p-i-n solar cells. *Appl. Phys. A Mater. Sci. Process.* **2004**, *79*, 1–14.

(46) Zhang, F.; Bijleveld, J.; Perzon, E.; Tvingstedt, K.; Barrau, S.; Inganäs, O.; Andersson, M. R. High photovoltage achieved in low band gap polymer solar cells by adjusting energy levels of a polymer with the LUMOs of fullerene derivatives. *J. Mater. Chem.* **2008**, *18* (D), 5468.

(47) Cates, N. C.; Gysel, R.; Beiley, Z.; Miller, C. E.; Toney, M. F.; Heeney, M.; McCulloch, L.; McGehee, M. D. Tuning the properties of polymer bulk heterojunction solar cells by adjusting fullerene size to control intercalation. *Nano Lett.* **2009**, *9* (12), 4153–4157.

(48) Larsen-Olsen, T. T.; Andersen, T. R.; Dam, H. F.; J??rgensen, M.; Krebs, F. C. Probing individal subcells of fully printed and coated polymer tandem solar cells using multichromatic opto-electronic characterization methods. *Sol. Energy Mater. Sol. Cells* **2015**, *137*, 154–163.

(49) Hadipour, A.; De Boer, B.; Wildeman, J.; Kooistra, F. B.; Hummelen, J. C.; Turbiez, M. G. R.; Wienk, M. M.; Janssen, R. a J.; Blom, P. W. M. Solution-processed organic tandem solar cells. *Adv. Funct. Mater.* **2006**, *16*, 1897–1903.

(50) An, Q.; Zhang, F.; Li, L.; Wang, J.; Zhang, J.; Zhou, L.; Tang, W. Improved Efficiency of Bulk Heterojunction Polymer Solar Cells by Doping Low Bandgap Small Molecule. *ACS Appl. Mater. Interfaces* **2014.**

(51) Blom, P. W. M.; Mihailetchi, V. D.; Koster, L. J. A.; Markov, D. E. Device physics of polymer:Fullerene bulk heterojunction solar cells. *Adv. Mater.* **2007**, *19* (12), 1551–1566.

(52) Singh, E.; Nalwa, H. S. Stability of graphene-based heterojunction solar cells. *RSC Adv*. **2015**, *5* (90), 73575–73600 DOI: 10.1039/C5RA11771B.

(53) You, J.; Dou, L.; Hong, Z.; Li, G.; Yang, Y. Recent trends in polymer tandem solar cells research. *Prog. Polym. Sci.* **2013**, *38* (12), 1909–1928.

(54) Heeger, A. J. Semiconducting polymers: the Third Generation. *Chem. Soc. Rev*. **2010**, *39* (7), 2354–2371.

(55) Hermenau, M.; Riede, M.; Leo, K.; Gevorgyan, S. A.; Krebs, F. C.; Norrman, K. Water and oxygen induced degradation of small molecule organic solar cells. *Sol. Energy Mater. Sol. Cells* **2011**, *95* (5), 1268–1277.

(56) Kim, I.; Kwak, S. W.; Ju, Y.; Park, G. Y.; Lee, T. M.; Jang, Y.; Choi, Y. M.; Kang, D. Roll-offset printed transparent conducting electrode for organic solar cells. *Thin Solid Films* **2015**, *580*, 21–28.

(57) Krebs, F. C.; Tromholt, T.; Jørgensen, M. Upscaling of polymer solar cell fabrication using full roll-to-roll processing. *Nanoscale* **2010**, *2* (6), 873–886.

(58) Krebs, F. C. Fabrication and processing of polymer solar cells: A review of printing and coating techniques. *Sol. Energy Mater. Sol. Cells* **2009**, *93*, 394–412.

(59) Krebs, F. C. Polymer solar cell modules prepared using roll-to-roll methods: Knife-over-edge coating, slot-die coating and screen printing. *Sol. Energy Mater. Sol. Cells* **2009**, *93* (4), 465–475.

(60) Kim, H. S.; Dhage, S. R.; Shim, D. E.; Hahn, H. T. Intense pulsed light sintering of copper nanoink for printed electronics. *Appl. Phys. A Mater. Sci. Process.* **2009**, *97* (4), 791–798.

(61) Ryu, J.; Kim, H.-S.; Hahn, H. T. Reactive Sintering of Copper Nanoparticles Using Intense Pulsed Light for Printed Electronics. *J. Electron. Mater.* **2011**, *40* (1), 42–50.

# CHAPTER 3

# RESULTS AND DISCUSSION

## 3.1 Overview

The polymer solar cells based on P3HT and PCBM are known as one of the most promising donor-acceptor systems in the bulk heterojunction solar cells. This is mainly because of their low cost and easy solution processing. However, there are some shortcomings, which are limiting this system's ability to become commercially scalable. Some of those limitations are: 1) Low power conversion efficiency, 2) Stability of fabricated devices, 3) Reproducibility of the cells, and 4) Viability for commercial fabrication. Numerous research papers have been published to solve these limitations.[1] Importantly, the efficiency has reached up to 5%.[2] However, further work needs to be done to improve not only the device efficiency but also the device stability and large-scale fabrication.

The research goal of this thesis is to make highly efficient and stable P3HT: PCBM-based BHJ solar cells and to investigate their fabrication on the large-scale. The power conversion efficiency for an organic solar cell mainly depends on the active layer morphology. Major manipulation techniques to improve morphology introduced in the past include thermal and solvent annealing techniques. In this thesis work a novel solvent annealing technique was introduced to improve the power conversion efficiency of P3HT:PCBM based solar cells. Also, we explored the possibility of replacing the cathode material with low cost, and stable copper cathode. Furthermore, the possibility of large-scale solar cell fabrication was evaluated using the roll-to-roll fabrication facilities at the Conn Center at the University of Louisville.

During this research work, the following four tasks were performed:

(i) Fabrication and evaluation of photovoltaic performance of P3HT:PCBM based devices.

(ii) Optimization of the active layer morphology using a novel solvent annealing technique.

(iii) Developing a new cathode material and evaluating photovoltaic performance.

(iv) Fabrication of a scale up prototype using roll-to-roll printing technique.

### 3.2 Fabrication and evaluation of photovoltaic performance of P3HT:PCBM based devices

In the present work, a set of P3HT: PCBM based photovoltaic cells with the device configuration of Glass/ITO/PEDOT: PSS/P3HT: PCBM/Ca/Al were fabricated. PEDOT:PSS is poly (3,4-ethylenedioxy- thiophene) polystyrene sulfonate used as a hole conducting layer. After coating the PEDOT:PSS layer, P3HT:PCBM active layer was coated using the spin coating method while exposing it to IR light. This simultaneous spinning and exposure to IR radiations helps to achieve high thickness with uniformity. During the spinning, heat from IR radiation helps to accelerate the evaporation of a solvent from the active layer. The accelerated evaporation of a solvent facilitates the active layer solution to dry quickly and form a uniform layer on the substrate. During these fabrication processes, we have encountered formation of pin-holes on the active layer substrate if the spin-coating proceeds without exposure to IR light. We have used 1,2-dichlorobenzene as a solvent to dissolve the P3HT:PCBM blend solution. After coating the active layer it was allowed to dry for 20 minutes under nitrogen environment. The devices prepared in this manner were subjected to accelerated-solvent vapor

annealing, in which devices were kept inside high vapor concentration environment. Figure 3.1 shows the set up used for the solvent annealing process. First, the solvent chamber was saturated with dichlorobenzene solvent vapors followed by active layer coated substrates were carefully introduced on to a stage inside the solvent chamber. After, 7 minutes time interval, substrates were removed from the solvent chamber and allowed to dry in the nitrogen filled glovebox for 20 minutes.

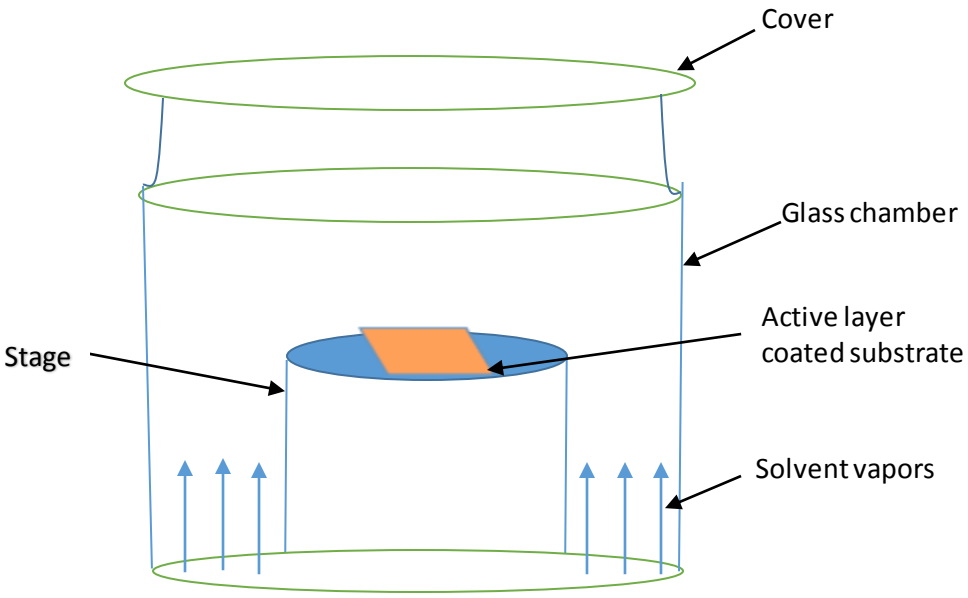


**Figure 3.1**: solvent annealing process

It was evidenced by previous research that solvent vapors helps in morphology improvement of P3HT:PCBM bulk heterojunction layer. Typically, solvent vapors facilitates in P3HT polymer crystal growth and PCBM molecule aggregation. Verplaugeun et al. showed that solvent vapor annealing provides molecular mobility within the molecular and polymer chain structure that facilitate local rearrangement among the polymer chains and PCBM molecules.[3] Solvent vapors do not fully dissolve

the components, but due to the high vapor concentration in the environment, solvent vapor diffuses through P3HT-PCBM components. As a result, each component rearranges to ordered nanoscale structures, which are called as nano-phase segregation. During this process, P3HT component exhibits a crystal growth and PCBM molecules rearrange closely together to form aggregates due to the increased mobility of solutes. This crystal growth and aggregation of the active layer film revealed by atomic force microscopy (AFM), which will be discussed in the later section. Verplaugeun et al. characterized the active layer film using glazing incidence wide angle X-ray scattering technique and confirmed that the solvent vapor annealing significantly improved the P3HT crystallinity, PCBM crystallinity, and nanoscale phase segregation of P3HT:PCBM blend.[3]

In our case, we used 1,2-dichlorobenzene as our solvent for the solvent vapor annealing process as 1,2-dichlorobenzene shows the high diffusion rate of the polymer and PCBM due to its high boiling point. High boiling point solvent evaporates slowly from the active layer, therefore it provides more time to self-organize the molecules in the active layer with equilibrium morphology. Pre- solvent annealing benefits to grow P3HT and PCBM crystals freely in the active layer since there is no disturbance from the cathode because this process performs before the cathode deposition step.

In this set of experimental results, a total of 20 devices were fabricated with the pre-electrode solvent annealing method. A layer of aluminum was coated on each devices as a cathode material. Table 3.1 shows the photovoltaic characteristics of the fabricated devices. The highest short circuit current density ($J_{sc}$) achieved with this study was 32.04 $mA/cm^2$ with the highest efficiency of 9.20% for champion cells.

**Table 3.1:** Photovoltaic Characteristics of solar cells fabricated by pre-fabrication solvent annealing method

| Sr. No | Short Circuit Current $J_{SC}$ (mA/cm$^2$) | Open circuit voltage $V_{OC}$ (V) | Fill Factor FF (%) | Power conversion efficiency PCE (%) |
|---|---|---|---|---|
| 1 | 29.35 | 0.65 | 34.33 | 6.61 |
| 2 | 24.36 | 0.65 | 36.09 | 5.82 |
| 3 | 25.14 | 0.63 | 35.38 | 5.64 |
| 4 | 5.50 | 0.61 | 48.20 | 7.49 |
| 5 | 20.79 | 0.61 | 51.95 | 6.58 |
| 6 | 27.90 | 0.61 | 45.20 | 7.71 |
| 7 | 21.15 | 0.59 | 45.21 | 5.73 |
| 8 | 32.04 | 0.63 | 45.60 | 9.20 |
| 9 | 26.57 | 0.61 | 34.60 | 5.67 |
| 10 | 27.84 | 0.61 | 36.35 | 6.16 |
| 11 | 39.10 | 0.61 | 36.04 | 8.44 |
| 12 | 23.94 | 0.61 | 38.45 | 5.67 |
| 13 | 35.46 | 0.61 | 36.71 | 7.81 |
| 14 | 22.69 | 0.60 | 37.93 | 5.16 |
| 15 | 32.32 | 0.60 | 39.19 | 7.60 |
| 16 | 22.98 | 0.59 | 42.39 | 5.74 |
| 17 | 26.53 | 0.61 | 41.28 | 5.98 |
| 18 | 22.30 | 0.61 | 38.84 | 5.33 |
| 19 | 18.75 | 0.63 | 35.08 | 6.62 |
| 20 | 21.01 | 0.61 | 42.84 | 7.13 |

Similar annealing methods have employed in the past and was evidenced from AFM and glazing incidence wide angle X-ray scattering (GIWAXS) that, the solvent vapor annealing significantly improves the nanoscale morphology of P3HT:PCBM donor-acceptor components. We have evaluated the nanoscale morphology using AFM to correlate the photovoltaic performance summarized in Table 1. Highest efficiency we have achieved from these cells was 9.2% with a fill factor of 45% under 1 sun illumination and 1.5 AM while the average PCE was found to be 6.60% with a standard deviation of 1.12%. It is important to note that the limiting factor for higher efficiency is the lower fill factor, although the current density is considerably high. Fill factor denotes

the quality of a diode, which is affected by the film uniformity and nanoscale phase segregation.[4] In our device characterizations, fill factors are in the range of 35-45%, which is considered as low compared to the literature reported fill factor for P3HT/PCBM devices.[5] Therefore, more focus needs to be put on increasing the fill factor of these devices in our future studies. It can be increased by improving the active layer morphology. Previous studies have shown that an optimum concentration of an active layer solution needs to be optimized to achieve higher power conversion efficiency. Radbeh et al. studied the effect of concentration of an active layer on the power conversion efficiency of solar cells.[6] They found that up to certain limit, higher concentrations significantly improve the efficiency.[6] However, at a certain limit of the active layer concentration hampers the device performance. At very high concentrations donor-acceptor components are tightly packed within the active layer and eliminates the free movement of individual components to yield a better phase segregation. As a result at higher concentration, well-defined nano-phase morphology is limited although the donor-acceptor interfacial area increases. It was speculated that optimum concentration maintains to compromise nanoscale domain sizes and surface area of the donor and acceptor components. We have optimized the concentration of the active layer in our test devices to 37.5 mg/mL of the blend. This concentration is towards the high end compared to the typical active layer blends concentrations used in the literature.

In our research work, we have optimized the active layer thickness at 170-200 nm. The optimum thickness of the active layer was obtained by optimizing the spin rate and IR intensity. Increasing spin rate causes rapid dispersion of the dispensed solution from the center of the surface towards the periphery. Also, spin coating under IR

illumination facilitates accelerated solvent evaporation, which results in smooth homogenous thin film. We have optimized the spin rate at 2000 rpm for the active layer blend solution and IR lamp intensity was maintained at 45 W. The IR lamp was kept at 7 inches from the substrate surface vertically and its power was regulated with a power controller knob. It is important to maintain the IR lamp intensity at particular intensity value. The thickness can also be correlated with the IR lamp intensity. More intense light would cause rapid evaporation during the film formation and would provide a higher thickness. However, film destruction was observed at IR intensities higher than 55 W due to the high heat from IR radiation. As a result, optimized conditions for an uniform film with improved thickness are 45 W IR lamp intensity kept vertically at 7 inches from the device surface along with the spin rate of 2000 rpm. Figure 3.2 shows J-V curves of devices fabricated by solvent annealing method.

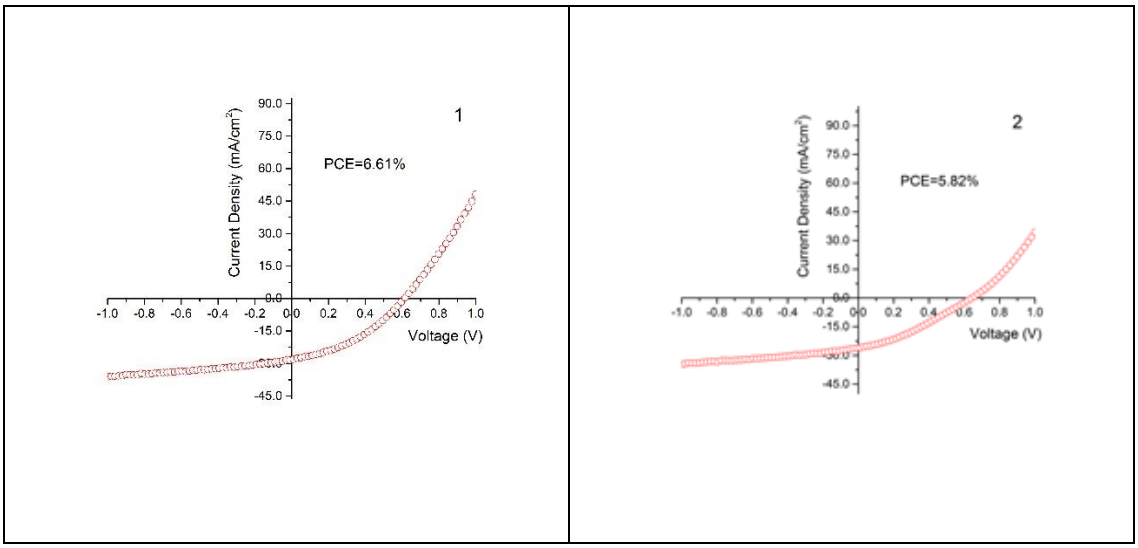

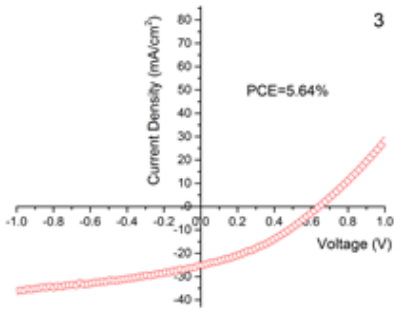
3
PCE=5.64%
Current Density (mA/cm²)
Voltage (V)

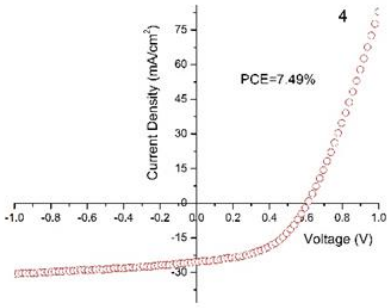
4
PCE=7.49%
Current Density (mA/cm²)
Voltage (V)

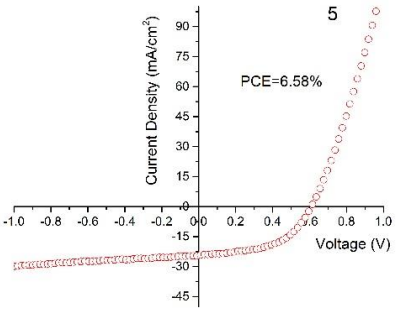
5
PCE=6.58%
Current Density (mA/cm²)
Voltage (V)

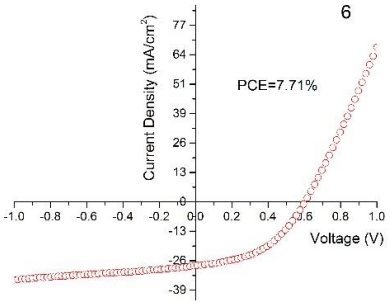
6
PCE=7.71%
Current Density (mA/cm²)
Voltage (V)

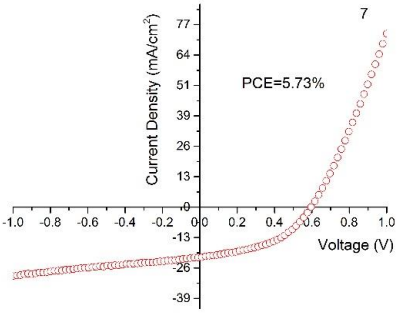
7
PCE=5.73%
Current Density (mA/cm²)
Voltage (V)

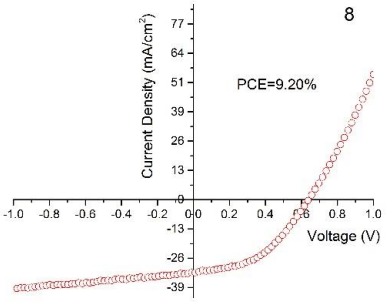
8
PCE=9.20%
Current Density (mA/cm²)
Voltage (V)

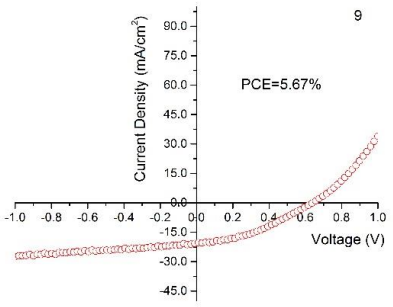
9
PCE=5.67%
Current Density (mA/cm$^2$)
Voltage (V)

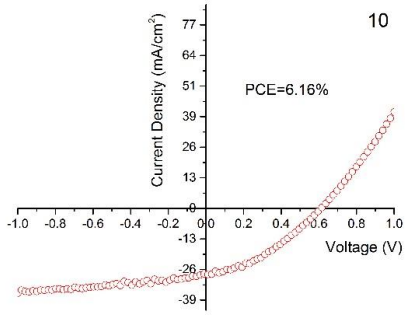
10
PCE=6.16%
Current Density (mA/cm$^2$)
Voltage (V)

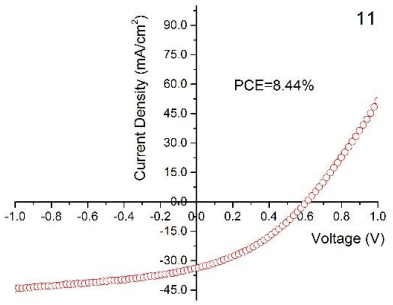
11
PCE=8.44%
Current Density (mA/cm$^2$)
Voltage (V)

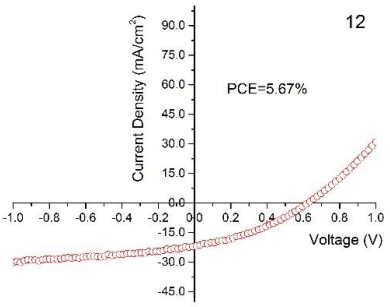
12
PCE=5.67%
Current Density (mA/cm$^2$)
Voltage (V)

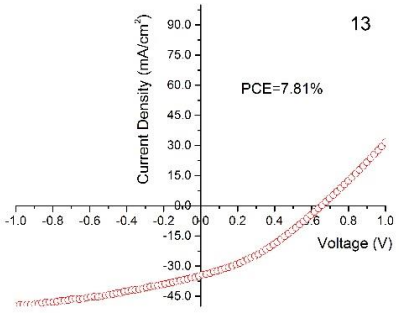
13
PCE=7.81%
Current Density (mA/cm$^2$)
Voltage (V)

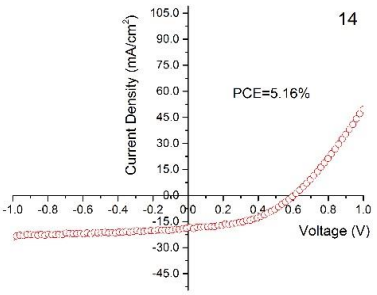
14
PCE=5.16%
Current Density (mA/cm$^2$)
Voltage (V)

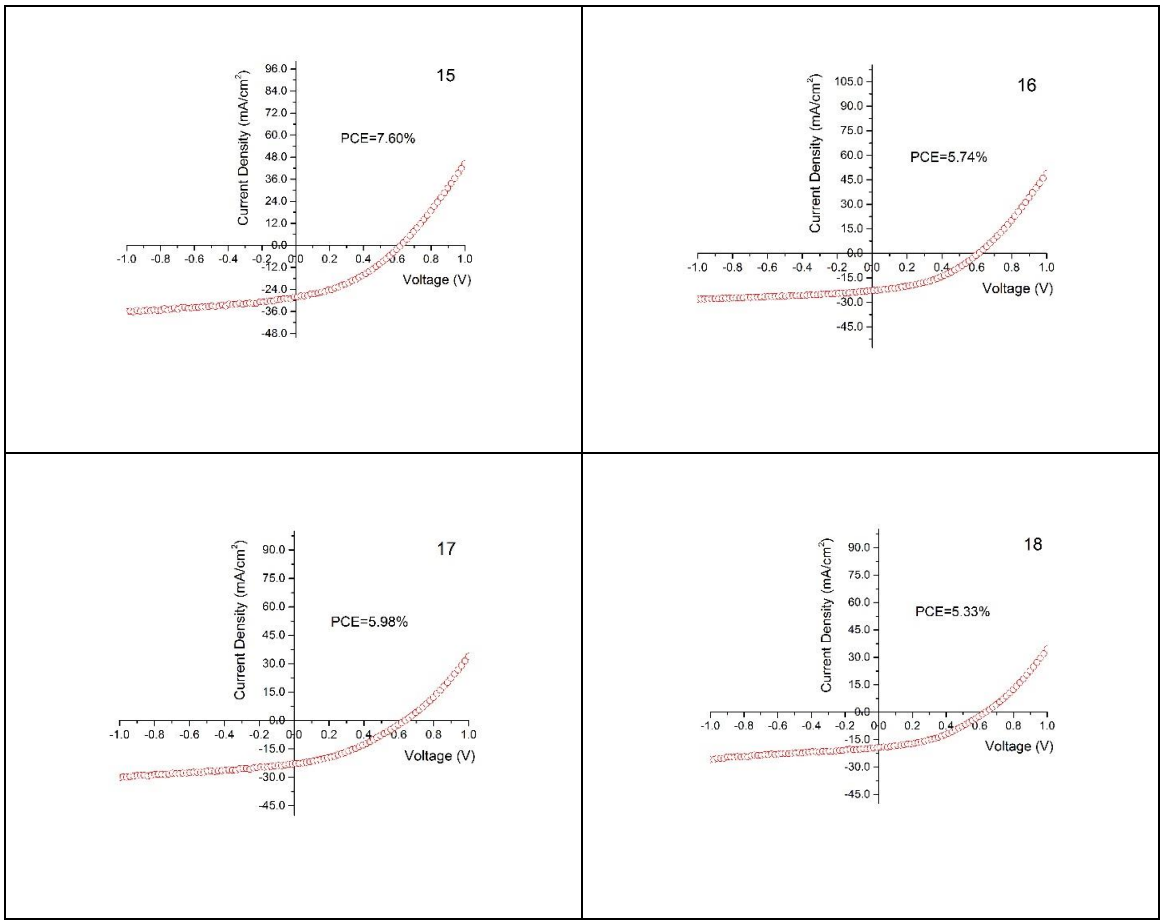


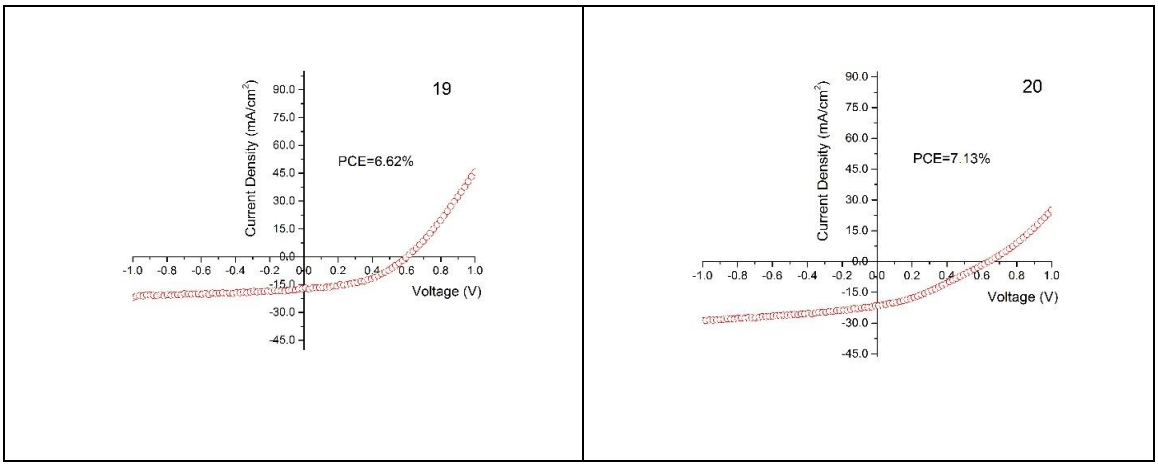


**Figure 3.2:** J-V curves of solvent annealed devices under illumination (Devices 1-20)

### 3.2.1 Analysis of film thickness and morphology using SEM:

Morphology of the active layer blend plays a major role in device efficiency as the charge carriers generated within the donor-acceptor interface need to move freely to the opposite electrodes.[7] According to previously published work, increasing the film thickness can improve light absorption.[8] Gang Li et al. have shown that significant improvement in the power conversion efficiency can be achieved by increasing the active layer thickness.[9] Islam et al. also demonstrated that there was an enhanced light absorption as the thickness of an active layer increases. However, high thickness of the active layer can limit the transparency. Therefore, the optimum thickness is one of the key-enabling factors to improve the device efficiency.

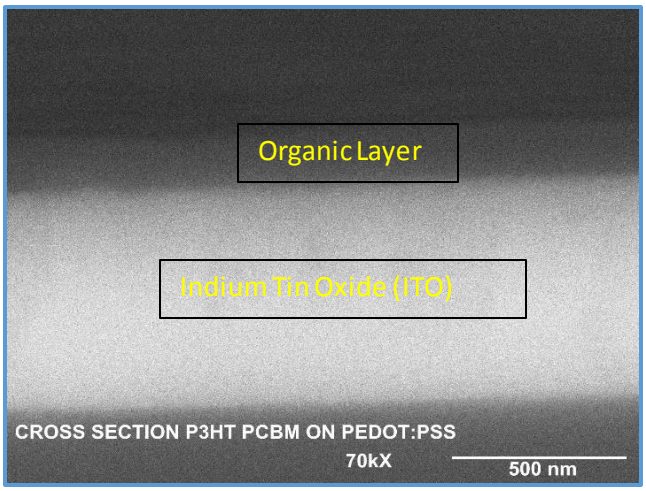


**Figure 3.3:** SEM BEI image of cross section of a device

The active layer film thicknesses of test devices fabricated in this study were obtained from a scanning electron microscope (SEM) using back-scattered electron imaging (BEI). Figure 3.3 is the cross section SEM image of a device showing the

organic layer and ITO layer. Devices were fractured gently under nitrogen and mounted vertically on sample mounting stub. In a typical procedure, samples were scored with a diamond scribe on the uncoated slide, cooled in liquid nitrogen followed by gently fracturing the glass and film beneath the score. The fractured surface was mounted face-up on a stub and viewed under SEM at 20 kV in low vacuum using backscattered electron detector. The detector was set to control the brightness, which is related to the density and atomic number of materials. We have selected a high efficiency device for the measurement of the thickness with SEM analysis. The active layer thickness was found to be ~170 nm. The thickness of the organic layer was measured using a tool in the SEM software.

### 3.3 Optimization of the active layer morphology using a novel solvent annealing technique.

Significant amount of research shows that controlling the active layer morphology is a successful strategy to improve device efficiency.[10] In the literature, non-annealed P3HT:PCBM devices have reached up to 3.63% efficiency while solvent and thermal annealed devices have reached up to 5.40%.[11] Importantly, solvent treatment on organic photovoltaics has improved phase segregation in the BHJ active layer.[12] Considering this concept, we have applied a solvent annealing method to improve the morphology of the active layer in our devices and studied the film morphology using AFM analysis, which will be discussed in section 3.3.1.

#### 3.3.1 Analysis of Film Morphology using AFM

**T**he active layer morphology was studied on AFM prior to the deposition of cathode material. In this analysis, the active layer was coated on PEDOT-PSS coated ITO

glass substrate. Although, PEDOT:PSS layer was present beneath the active layer during the analysis, we speculate that the surface roughness change in the active layer reflects the inner morphology of an active layer. The atomic force microscope is a very high resolution scanning probe microscope which is used with contact mode on the active layer surface.[13] This microscope measures the force between a probe and the surface of a sample. The probe is a nanoscale sharp tip that has capability of dragging across the surface of the sample in a raster pattern and deflection in the tip. The resulted topography of the surface is measured by the detector. The signals are then converted into an image representing nanoscale variations on the surface. We have optimized the parameters such as I-gain, P-gain, range of cantilever, and the scanned area of the AFM instrument during our analysis. Major parameters subjected to change include I-gain 70%, P-gain 72%, range of cantilever-2.5 μm, area scanned 10 μm X 10 μm, scanning resolution 1024 points/lines, and scanning speed 0.7 lines/sec. The average surface roughness ($R_a$) can be calculated from the software, which reflects the irregularities noted by the probe on the image. The AFM image shown in Figure 3.4 was processed on Gwyddion software to determine the average roughness of the films. The average roughness for the thin films in our devices was 6.51 nm.

In the literature, Li et al. have shown the effect of solvent annealing on the morphology using AFM. They casted a P3HT:PCBM film on glass and analyzed the film using AFM.[14] They have observed a significant improvement in the roughness of the film after solvent annealing substrate. Improvement in the roughness of the film was also studied by Bertrand et al., they argued that the roughness improvement was due to vertical phase segregation of grown polymer crystallites.[15] Similarly, Dante et al. studied

conductive AFM to evaluate the charge transfer through the active layer film and on the surface of the film. This study was performed in the active layer film before and after solvent annealing.[16] They have found that the improvement in charge transfer takes place through the film and on the surface. They speculated that this improvement was observed as a result of improved ordered structure of P3HT-PCBM components. However, in both of these studies, the average roughness values achieved are limited to 0.2 to 2 nm. In our case, high average roughness value may be due to improved morphology resulting from novel solvent annealing method. However, it is necessary to perform further analysis by separating the active layer from other layers of test devices to conclude that enhanced film morphology is the key enabling factor for higher thickness.

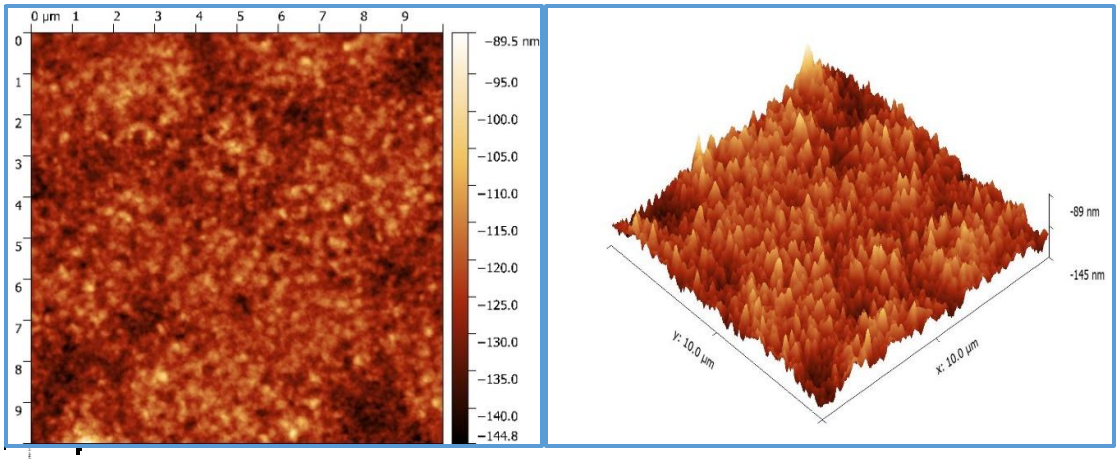


**Figure 3.4:** (Left) Two dimensional 2D AFM topography image of a solvent annealed device with scan area 10 µm X 10 µm; (Right) Three dimensional 3D AFM topography image with scan area 10 µm X 10 µm.

In AFM, I-gain and P-gain values are the feedback control parameters. Setting of I-gain and P-gain values depends upon surface variation (topography). Generally, I-gain and P-gain values are set to lower for rough surface measurements, where as those values

should be set to high for smooth surface measurements.[17] However, this setting also depends upon other factors such as sharpness of the tip and surface of material to be analyzed.[17] P3HT:PCBM layer is a relatively smooth surface, therefore, for the analysis of P3HT:PCBM blend layer surface, we have obtained I-gain 70% and P-gain 72%. It is important to note here, we have not observed noise in the feedback display up to 90% I-gain.

As depicted in Figure 3.4 high phase segregation was observed with solvent annealed devices. These segregated areas account for increase in the total surface area of the active layer blend, which enables improved hole-electron mobility.

Important mechanism involved in the process of solvent annealing is the crystal growth in P3HT domains. We have observed this growth from AFM images, which reflect the enhancement in film roughness. The variation in the topography of the active layer surface indicates the crystal growth. Furthermore, in order to identify the nucleation sites, higher concentration areas of P3HT and PCBM in the BHJ layer were analyzed. In the AFM image depicted in Figure 3.4, local sinks can be observed on the surface of the film. These are actually P3HT and PCBM depleted regions, showing less probable area for nucleation. Ideally, during solvent annealing, PCBM diffuses through BHJ matrix regions to explicit growth fronts. These growth fronts and depleted regions account for surface variation and thus roughness value gives an estimate for that surface variation across the scanned area. In Figure 3.4, three-dimensional and two-dimensional AFM topography images are depicted. Brighter spots show peaks, and darker spots show lowland or valleys in the surface of a BHJ film. The corresponding AFM topography images and color height scale reflects this variation.

We have studied the morphology of an active layer using AFM when PEDOT:PSS layer was already present beneath it. Therefore, the roughness we have achieved in this analysis is a collective layer roughness. We speculate that the roughness of the active layer film might have been affected by the collective roughness of PEDOT:PSS layer and ITO layer. Therefore, we propose further improvement can be done to obtain an accurate roughness of the active layer film by separating the active layer from the device surface.

### 3.4 Developing a new cathode material and evaluating photovoltaic performance

Aluminum is a prominently used metal cathode layer for organic based solar cells. However, power conversion efficiencies of the organic-based solar cells deteriorate with time in air and one of the main reasons is the oxidation of a metal cathode layer. Therefore, new materials are needed to replace the existing less stable cathode. Copper has a high work function and is thus more stable compared to aluminum.[18] Moreover, it is cheap and easy to apply due to its mechanical properties compared to other metal counterparts. These copper films have also shown transparency to some extent.[19] Therefore, to achieve our next objective, we have replaced the cathode layer with copper metal. Before the application, we measured the conductivity of evaporated copper using a two probe method. The potential applicability of copper as a cathode material for P3HT:PCBM based devices were also evaluated.

#### 3.4.1 Determination of Conductivity of Copper used as Cathode in Solar Cell

Copper beads were evaporated onto the glass surface and conductivity was measured on a cross-sectional area using a two-probe method. The conductivity measurements were performed using a Keithley 2400 sourcemeter.. Voltage was swept

from -1 to 1 V and corresponding current was measured. As expected, the resulting curve shows purely ohmic nature having much less resistance. Figure 3.5 shows the I-V plot for evaporated the copper layer on a glass substrate.

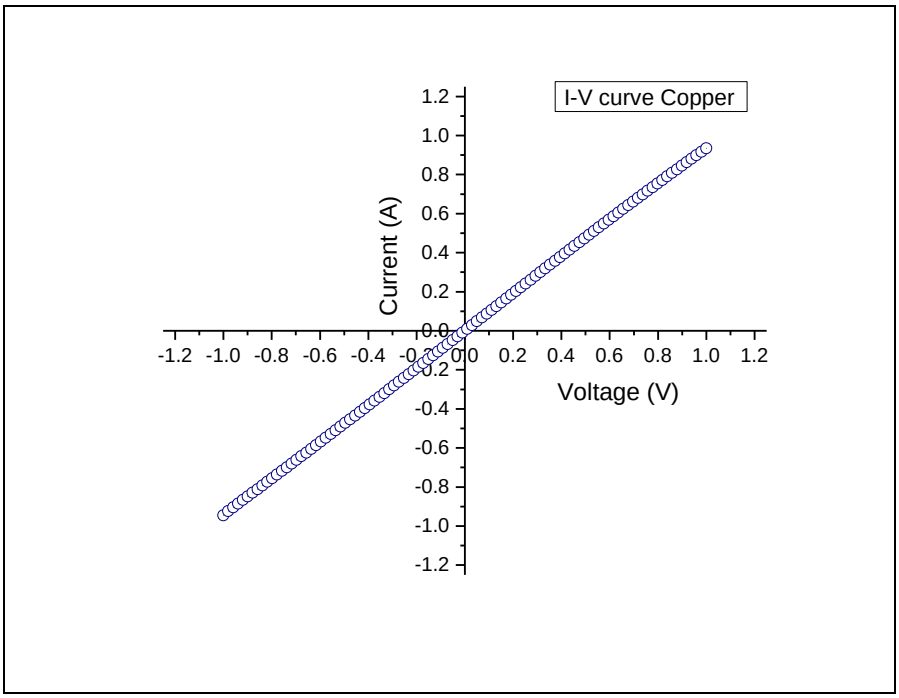


**Figure 3.5:** A selected I-V curve of a copper beads coated substrate

The resistivity value was found to be 1.05 X $10^{-7}$ Ω·cm with the calculated conductivity value of 9.51 X $10^{6}$ S/cm. The conductivity obtained is less compared to the reported value.[20] This may be due to the two-probe method used for our analysis. Typically, the four probe method is used for resistance or conductivity measurements, in which current is sent through two probes and the corresponding voltage is measured with two different probes. The voltage drop in the current wires does not contribute error to the voltage measurement. There is a very low current flow in the voltage sense wires. However, with two-probe technique, the voltage drop from the current flow will not be

separable from the voltage drop in the device under testing, which may cause some deviation in the measurement.

### 3.4.2 Incorporation of copper as a cathode for device fabrication

Generally, organic photovoltaics are fabricated with one of the metals as a cathode or anode, regardless of the device architecture. In a normal architecture, a high work function transparent electrode such as ITO works as a hole collecting layer (an anode). Similarly, a low work function non-transparent metal electrode works as an electron collecting layer or a cathode. Using the solvent annealing technique, we have made P3HT: PCBM based devices with conventional architecture using aluminum as a cathode. However, aluminum is not stable in ambient conditions due to its low work function which results in oxidation in the presence of oxygen atmosphere and can readily convert into poor conductive aluminum oxide ($Al_2O_3$).[21] Therefore, the photovoltaic performance of an organic solar cell rapidly deteriorates on exposure to air with time. Previous research has shown that the degradation of typical BHJ device architecture upon exposure to air longer time period.[22]

We have fabricated 4 devices replacing aluminum with a copper cathode with a configuration of ITO/PEDOT:PSS/P3HT:PCBM/Ca/Cu, following the same procedure as we have followed for our champion aluminum coated devices. Table 3.2 shows the photovoltaic characteristics of the devices with power conversion efficiencies. Maximum power conversion efficiency achieved with copper, as the cathode is 8.23% compared to aluminum which was 9.20%. We can relate this high efficiency with film morphology rather than the change of an electrode. Aluminum and copper have almost equal work functions and calcium is the primary contact from organic-to-metal flow of charge

carriers. It is important to note here that copper evaporation is faster and produces less heat while evaporation, which increases reproducibility compared to that of aluminum. Aluminum evaporation was conducted on a tungsten filament mounted on two oppositely charged electrodes; these electrodes apply voltage across the tungsten filament and cause heating. Aluminum mounted on the filament makes uneven contact with the filament, causing an uneven heat gradient or over heating of the filament. Thermal radiations from the filament heat the devices, and this causes defects in the active layer film and affects the device performance.

In the case of copper evaporation method, copper beads were mounted on the molybdenum boat and high voltage was applied through the boat. The melting of copper beads is relatively faster and evaporation is smooth. This helps retained steady heating and lower temperature evaporation, resulting in an even rate of evaporation. Therefore it provides fewer chances of defects in the devices.

**Table 3.2:** Photovoltaic Characteristics of solar cells fabricated by using copper as a cathode

| Sr. No | Short Circuit Current $J_{SC}$ (mA/cm$^2$) | Open circuit voltage $V_{OC}$ (V) | Fill Factor FF (%) | Power conversion efficiency PCE (%) |
|---|---|---|---|---|
| 1 | 30.18 | 0.6161 | 44.89 | 8.23 |
| 2 | 33.66 | 0.5959 | 40.81 | 8.18 |
| 3 | 33.16 | 0.6060 | 37.75 | 7.51 |
| 4 | 29.33 | 0.5959 | 39.60 | 6.92 |

The Figure 3.6, exhibits compared J-V curves for both aluminum and copper coated devices. These two devices show almost equal power conversion efficiencies of ~7.61% and other photovoltaic properties such as fill factor, $V_{oc}$ and $J_{sc}$. There are not significant improvements observed in other photovoltaic characteristics. It can be easily seen the J-V plot comparison between devices made from two different cathode

materials. However, there was a significant improvement in the reproducibility of working devices. This is due to the fact that during the thermal evaporation, control of aluminum evaporation is difficult compared to copper evaporation.

**Table 3.3:** Comparison of two devices with different cathode materials

| Sr. No | Short Circuit Current $J_{SC}$ (mA/cm$^2$) | Open circuit voltage $V_{OC}$ (V) | Fill Factor FF (%) | Power conversion efficiency PCE (%) |
|---|---|---|---|---|
| Aluminum | 32.32 | 0.6161 | 39.19 | 7.60 |
| Copper | 33.16 | 0.6060 | 37.75 | 7.51 |

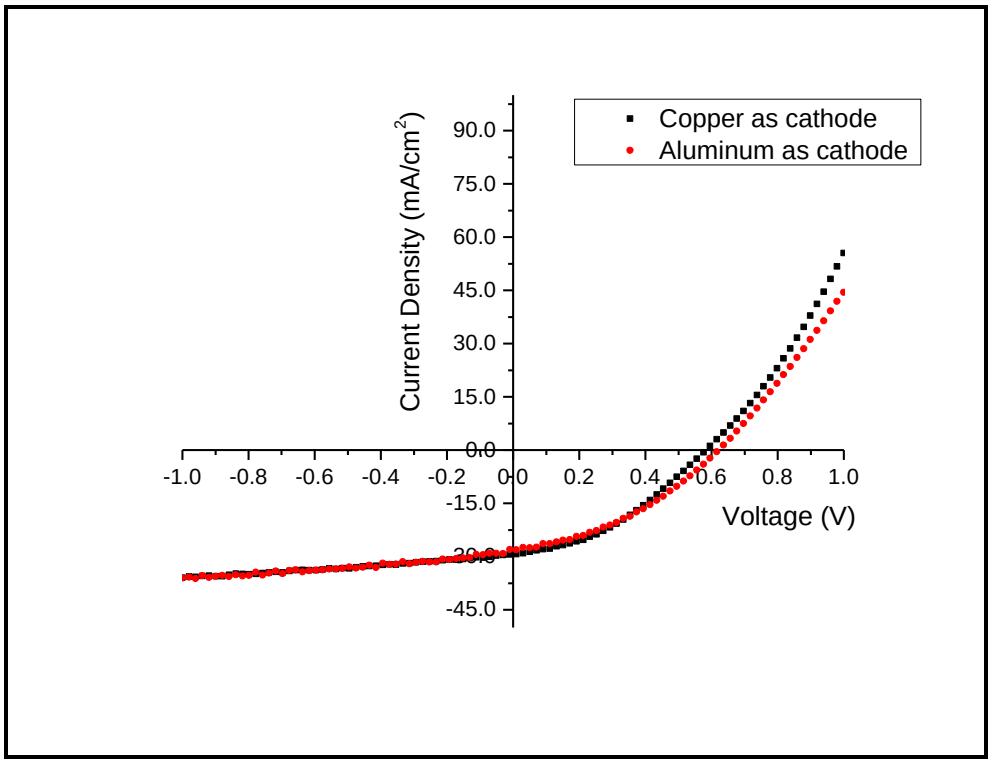


**Figure 3.6:** Comparison of J-V characteristics of devices coated with aluminum and copper.

### 3.4 Fabrication of a scale up prototype using roll-to-roll printing technique

Large-scale fabrication of organic solar cells from lab based techniques requires specific equipment and optimized processing techniques. We have used ultrasonic spray coating for large scale fabrication, similar to lab based spin coating. Instead of thermal evaporation, a screen printing method was used to deposit the cathode. Scale up studies were performed on an organic solar cell using lab synthesized and commercially purchased chemicals. However, lab made donor-acceptor compounds were used for this scale up study. Lab made P3HT was used as a donor compound and perylenediimide bridge-silane (PDIB-silane) was used as an acceptor. The following steps were performed during this study:

1. A trial ink was formulated to study ultrasonic spray parameters on large scale organic solar cell. Trial ink coated on flexible ITO coated plastic sheets.
2. With the optimized parameters from trial ink, PEDOT:PSS (hole conducting layer) was coated on flexible plastic sheets.
3. Donor-acceptor blend layer was deposited as the next layer on plastic sheets.
4. It was followed by deposition of copper nanoink, which is the cathode layer. Screen printing method was used to deposit the cathode nanoink.
5. Cathode deposited layer was sintered using Intense pulse light (IPL) sintering method.

Figure 3.7 shows the schematic diagram of a prototype used in our study.

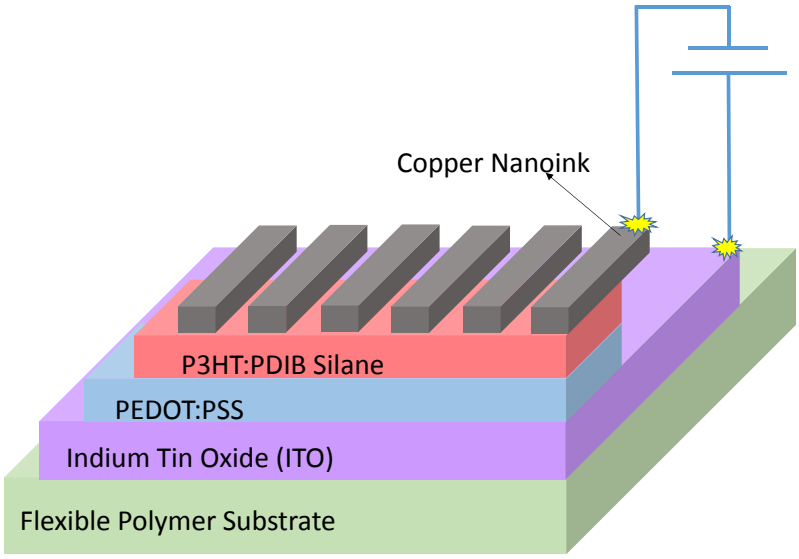


**Figure 3.7:** Device architecture for large scale fabrication study

### 3.4.1 PEDOT: PSS layer formation using ultrasonic spray

**Formulation of a trial ink:** Large scale operation requires high amounts of raw materials. Therefore, a trial ink was formulated initially to cut down the cost of raw materials. This trial ink was used to study ultrasonic spray parameters. With the optimized parameters from a trial ink, the PEDOT:PSS solution was coated on ITO-coated plastic sheets.

Homogenous deposition using ultrasonic spray depends upon the fluid properties of the solution used. One of the important properties of the solution is its viscosity. We have considered the assumption that a solution of similar fluid properties would give similar results when deposited by ultrasonic spray coating. Therefore, a PEDOT:PSS solution was subjected to viscosity measurement. With various trials, the following formulation gave the most optimal results: 10% ethylene glycol, 2% food dye, 60% ethanol and 28% water. Viscosity measurement comparison between PEDOT:PSS and the trial ink is given below.

**Table 3.4:** Viscosity measurement of PEDOT:PSS and Trial ink

| Material | Viscosity (cP) | Percentage level (%) | Spindle no. | rpm |
|---|---|---|---|---|
| PEDOT:PSS | 40 | 95 | 61 | 100 |
| Trial Ink | 54 | 90.4 | 61 | 100 |

**Selection of PEDOT:PSS-** Ultrasonic spray parameters depends upon the type of solution composition and particle concentration. PEDOT:PSS is commercially available in different grades that depend upon the conductivity of the charge carriers. For semiconductor applications, low conductivity PEDOT:PSS is used. PEDOT:PSS formulated for inject printing purposes was used for our ultrasonic spray study. Its composition is 1.3 wt.% PEDOT: PSS dispersed in water and alcohol. High water content in the depositing solution causes a wettability issue. When the solution was sprayed on plastic substrate due to the high surface tension, the droplets from ink jet printing repelled back and result in uneven film on the substrate. Water has a surface tension of 72 dynes/cm$^2$ while alcohols are in the range of 30-40 dynes/cm$^2$. Higher content of alcohol in the PEDOT:PSS enables the formation of a good film. Ultrasonic spray further reduces the kinetic energy of droplets sprayed on substrates. A lower kinetic energy would restrain the droplets from repelling back.

**Setting up parameters for ultrasonic spray:** As shown in the Table 3.5, ultrasonic spray control parameters were obtained for trial ink to get an uniform film. Later, the same parameters were applied and slightly tuned to get an uniform PEDOT:PSS film. Parameters significantly affecting the uniformity of film are motor speed, nozzle power, and flow rate. This should be noted that increasing the motor speed will reduce the

amount of solution deposited on the substrate. This happens due to covering a greater portion of the substrate area with a constant spray rate. Therefore changing the flow rate with respect to the speed of the motor was monitored.

While optimizing the parameters it was found that reducing the nozzle power changes the droplet size. This happens due to the fact that the nozzle power affects the degree of oscillation of the nozzle. The nozzle is connected to the ultrasonic transducers which are responsible for the degree of ultra-sonication achieved. It is important to mention here that, the droplet size determined by type of solution used. In this case, viscosity of PEDOT:PSS used was 30-40 cP, however, different solvents exhibit different droplet size depending on the viscosity and surface tension.

Usually, during ultrasonic spray coating, the small droplets fall on the surface of the substrate. These small droplets coalesce to form a big droplet, affecting the film uniformity. An ideal case would be a number of small droplets spreading uniformly with high density, avoiding coalescence. This can be improved by changing the speed of the motor by some extent. In our case, the substrates were subjected to heat treatment processes during spray coating. Substrates were kept on a hot plate during the spray coating to improve the uniformity of the film. Plastic substrates were kept on hot plate for 5 minutes at 150 $^{o}$C, facilitating a uniform layer after every 4 or 8 passes.

**Table 3.5:** Ultrasonic spray parameters for deposition of an active layer.

| | Sr. No. | Parameter | Optimized value for uniform layer |
|---|---|---|---|
| **Step motor parameters** | 1 | Stage speed | 15 mm/sec |
| | 2 | Stage distance | 120 mm |
| | 3 | No. of passes | 4 |
| | 4 | Pause between each pass | 0 Sec |
| **Ultrasonic spray control panel parameters** | 1 | Flow Rate | 2 mL/min |
| | 2 | Jet Force | 40 Lit/min |
| | 3 | Conveyer | 3 Ft/min |
| | 4 | Nozzle power | 3 Watts |
| | 5 | Spray on | 1 inch |
| | 6 | Spray off | 1 inch |
| | 7 | Stage height | 10.6 cm |
| | 8 | Spray Width | 2 inch |

Films started to show adequate uniformity when the annealing process was incorporated. However, after every 4 or 8 passes, removing the substrate from the spraying system became time consuming and was not suitable for roll-to- roll manufacturing of flexible polymer solar cells. Therefore, plastic substrates were kept on a hot plate at 150 $^{o}$C and performed an ultrasonic spray coating. This showed improved performance as well as significantly reduced time. Uniformity of the PEDOT: PSS coated film is confirmed by visualizing under a SEM and is shown in Figure 3.8.

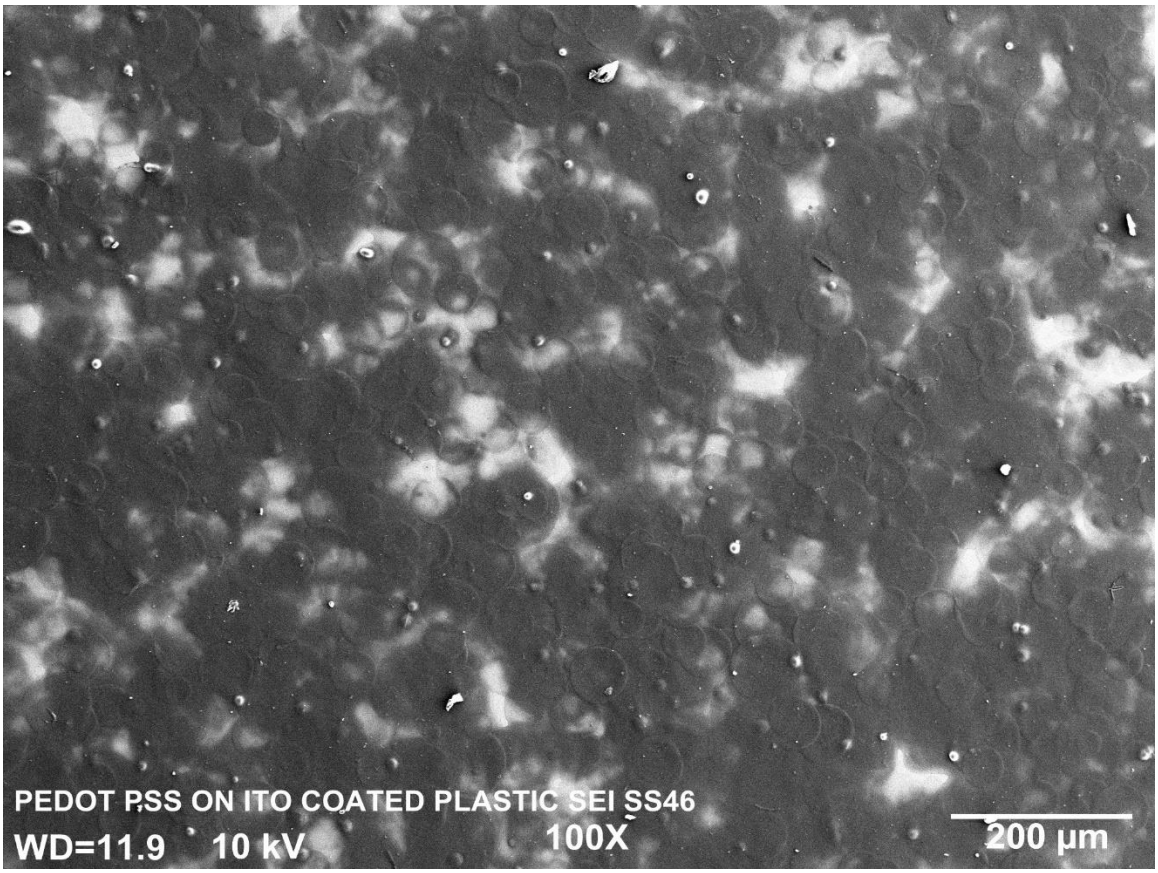


**Figure 3.8:** Ultrasonic spray pattern of PEDOT:PSS on ITO coated polymer

A few FTO coated plastic substrates are then coated with PEDOT:PSS with the optimized parameters, discussed above, in ambient conditions. It was found that FTO coated films showed the same degree of uniformity as evidenced by the SEM image in Figure 3.9. However, the film formed on FTO coated glass has revealed improved crystal growth. This may be due to thermal conductivity difference between flexible plastic and glass. Reduced rate of evaporation enhanced crystallization on FTO coated glass films.

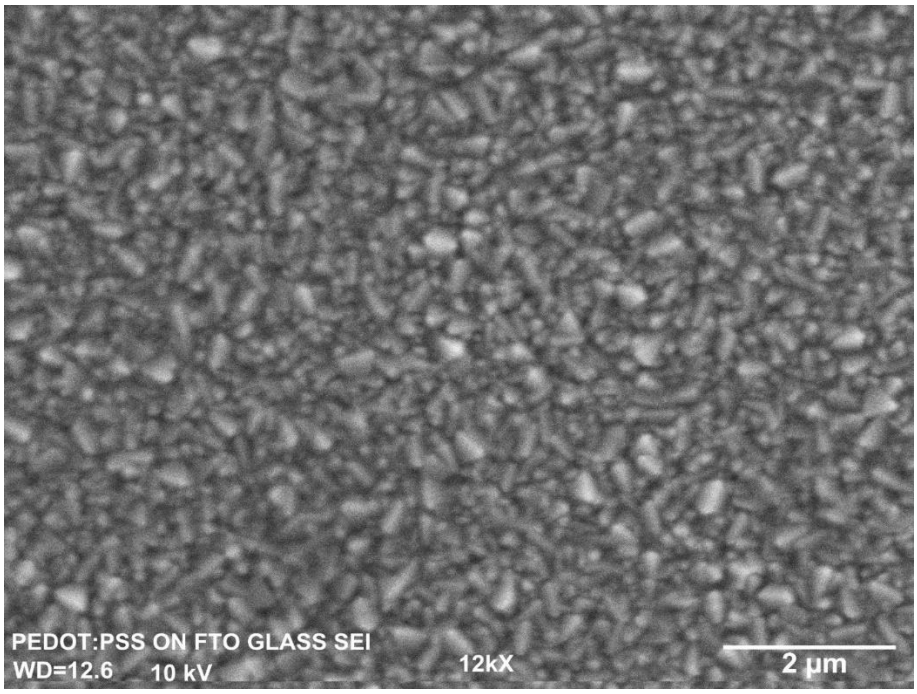


**Figure 3.9:** SEM image of PEDOT: PSS layer on FTO coated glass substrate

Notably, this fabrication processing needs to be done in an inert atmosphere. Due to non-availability of such a facility, we were constrained to make a prototype of a BHJ solar cell. The future potential area of research would be in the fabrication of this polymer cell in an inert condition.

### 3.4.2 Deposition of a photoactive Donor:Acceptor layer

Similar to PEDOT:PSS deposition with the ultrasonic spray technique, the active layer was deposited on the PEDOT:PSS layer. The active layer used for this study is a blend of a donor, P3HT and an acceptor, PDIB-silane. Both compounds were synthesized in house. Compounds were dissolved in 1, 2-dichlorobenzene, stirring separately overnight and later mixed together to form a blend. This blend was then used to coat an active layer on the PEDOT:PSS layer using the ultrasonic spray machine. The following

set of parameters gave a uniform layer, and the uniformity was observed under a light box.

**Table 3.6:** Ultrasonic spray parameters for deposition of an active layer.

| | Sr. No. | Parameter | Optimized value for uniform layer |
|---|---|---|---|
| **Step motor parameters** | 1 | Stage speed | 30 mm/sec |
| | 2 | Stage distance | 140 mm |
| | 3 | No. of passes | 4 |
| | 4 | Pause between each pass | 0 Sec |
| **Ultrasonic spray control panel parameters** | 1 | Flow Rate | 1 mL/min |
| | 2 | Jet Force | 40 Lit/min |
| | 3 | Conveyer | 3 Ft/min |
| | 4 | Nozzle power | 6 Watts |
| | 5 | Spray on | 1 inch |
| | 6 | Spray off | 1 inch |
| | 7 | Stage height | 13.5 cm |
| | 8 | Spray Width | 2 inch |

High evaporation rate of 1, 2-dichlorobenzene facilitates in rapid evaporation of the blend. After each set of 8 passes, substrates were subjected to thermal annealing at 100 ˚C for 5 minutes. Transparency of the cell reduces with increasing number of passes. After 56 passes, decent transparency was achieved with a homogenous film.

### 3.4.3 Deposition of a Cathode Layer

A cathode layer was deposited as a successive layer on active layer. Ink-form of copper nanoparticles were formulated by Dr. Thad Druffel's research group from the University of Louisville. This nanoink was deposited using a screen printing method. A screen printing block out was prepared using a blocking polymer. For this purpose, a 20 inch X 24 inch screen was taken and coated uniformly with blocking polymer, allowed to dry for a day, and then taken for UV curing. A stencil with the patterns was made using a graphics software kept below the screen to block UV rays forming the specific patterns shown in Figure 3.10. Different types of patterns were formed putting a varying number of stripes on the same substrate, giving a variety of choices during the process.

**Figure 3.10:** Stencil for screen printing

For screen printing, a mesh size of 200 is sufficient for the finer details in printing. For example, a 400 mesh size screen will give sharper details compared to 200 mesh size screen. Screens used for printing purposes are made from different materials. The most commonly used materials are polyester and aluminum. Polyester gives high

flexibility during the process and is easy to wash as well. Therefore, we used polyester for the screen printing of the cathode layer.

In the screen printing process, the time required for UV curing needs to be evaluated for a given plastomer, which is a photoactive polymer that solidifies upon UV irradiation. The screen was coated with the plastomer and was dried for a day. After drying, the screen is placed in an UV chamber. At one-minute time intervals, the extent to which the plastomers adhered to the screen was determined. The optimal UV curing time was found to be 2 minutes for a given plastomer.

After the preparation of a screen with the required pattern given in Figure 3.10, copper nanoink was printed on the active layer coated substrates. The layer of copper nanoink was deposited in a stripe form as a block out pattern. It was then dried at 100 °C for 10 minutes to get rid of any residual solvent. After drying the device, it was cooled to room temperature. Conductivity of the copper layer was measured with a two probe method using a Keithley 2400 sourcemeter. The average conductivity of the deposited layer was found to be $4.31 \times 10^4$ S/m which is three orders less than bulk copper metal conductivity, $5.96 \times 10^7$ S/m. Therefore, devices were subjected to intense pulse light sintering. Intense pulse light is a technique known to improve the conductivity of printed inks.

### 3.4.3 Intense Pulse Light (IPL) Sintering of a Cathode Nanoink

Substrates coated with copper nanoink were taken for intense pulse light (IPL) treatment. In the IPL treatment, an intense xenon lamp flash is used to irradiate the substrate. Due to the high intensity of flash light, copper nanoparticles melts to some extent. This leads to the reduction of inter-particle distances among copper nanoparticles

and thus increases the conductivity of the copper nanoink layer. The xenon lamp irradiates the light with wavelength range from 200 to 1100 nm. IPL treatment was carried out with three different parameters given below.

**Table 3.7**: Conductivity improvement using intense pulse light (IPL) treatment

| **Energy Applied** | **Time of exposure** | **Pulse width** | **Conductivity before IPL treatment (S/m)** | **Conductivity after IPL treatment (S/m)** |
|---|---|---|---|---|
| 30 J/cm$^2$ | 10 sec | 2 ms | 4.1 X 10$^4$ | 9.2 X 10$^4$ |
| 40 J/cm$^2$ | 10 sec | 2 ms | 2.8 X 10$^4$ | 1.1 X 10$^5$ |
| 50 J/cm$^2$ | 10 sec | 2 ms | 6.0 X 10$^4$ | 2.3 X 10$^5$ |

The flash light, within fractions of time, can sinter the layer due to its high intensity. It is important to note here that as the nanoparticle diameter decreases, the melting becomes more efficient. The diameter of 5 nm nanoparticles gave a decent conductivity for the copper layer. We have obtained different conductivity values under exposure to different intensities as shown in the Table 3.7**.** The average conductivity of the copper nanoink layer was found to be 1.18 X 10$^5$ S/m. However, it should be noted that after the screen printing, uncertainty lies in the conductivity due to poor metal layer formation during screen printing. Therefore, to obtain higher conductivity in the metal layer, a more uniform layer is desired.

IPL is a high intensity flash light and high energy as well. This may destroy or affect the polymer in short period of time. The present work of study limits to a short span of exposure of IPL. However, significant improvement in the conductivity of the film was observed with a short time period of 2 ms.

Importantly, the polymer substrates used are not stable at high temperatures. Heat sintering can damage polymer substrates. If thermally stable active layer molecules are

used (i.e. donor and acceptor) viability of IPL sintering extensively increases. Therefore, the IPL sintering is an excellent fabrication process for solar cell fabrication using low-temperature polymer substrates. In the course of IPL study, substrates used are polyethelene (PE) and polyethelene terephthalate (PET) which are not affected in the presence of high energy, considering their low melting point.

As reported in literature, it is known that IPL contains an excess amount of UV light with high intensity, which is shown in the spectrum for the IPL xenon lamp. This UV light affects the PEDOT:PSS and active layer which is a blend of P3HT and PDIB-silane, in this case. In the literature, it has been shown that the PEDOT:PSS film loses its texture on the surface and is known to happen due to the degradation by UV light. To overcome this, few alternatives are available, such as applying a UV filter or adding UV stabilizers in the mixture..

**References**


(1) Heeger, A. J. 25th anniversary article: Bulk heterojunction solar cells: Understanding the mechanism of operation. *Adv. Mater.* **2014**, *26*, 10–28.

(2) Scharber, M. C.; Sariciftci, N. S. Efficiency of bulk-heterojunction organic solar cells. *Prog. Polym. Sci.* **2013**, *38* (12), 1929–1940.

(3) Verploegen, E.; Miller, C. E.; Schmidt, K.; Bao, Z.; Toney, M. F. Manipulating the Morphology of P3HT–PCBM Bulk Heterojunction Blends with Solvent Vapor Annealing. *Chem. Mater.* **2012**, *24* (20), 3923–3931.

(4) Glatthaar, M.; Riede, M.; Keegan, N.; Sylvester-Hvid, K.; Zimmermann, B.; Niggemann, M.; Hinsch, a.; Gombert, a. Efficiency limiting factors of organic bulk heterojunction solar cells identified by electrical impedance spectroscopy. *Sol. Energy Mater. Sol. Cells* **2007**, *91* (5), 390–393.

(5) Servaites, J. D.; Ratner, M. a.; Marks, T. J. Practical efficiency limits in organic photovoltaic cells: Functional dependence of fill factor and external quantum efficiency. *Appl. Phys. Lett.* **2009**, *95*, 2009–2011.

(6) Radbeh, R.; Parbaile, E.; Bouclé, J.; Di Bin, C.; Moliton, a; Coudert, V.; Rossignol, F.; Ratier, B. Nanoscale control of the network morphology of high efficiency polymer fullerene solar cells by the use of high material concentration in the liquid phase. *Nanotechnology* **2010**, *21* (3), 035201.

(7) Campoy-Quiles, M.; Ferenczi, T.; Agostinelli, T.; Etchegoin, P. G.; Kim, Y.; Anthopoulos, T. D.; Stavrinou, P. N.; Bradley, D. D. C.; Nelson, J. Morphology evolution via self-organization and lateral and vertical diffusion in polymer:fullerene solar cell blends. *Nat. Mater.* **2008**, *7* (February), 158–164.

(8) Wang, F.; Wu, M. Z.; Wang, Y. Y.; Yu, Y. M.; Wu, X. M.; Zhuge, L. J. Influence of thickness and annealing temperature on the electrical, optical and structural properties of AZO thin films. *Vacuum* **2013**, *89* (December), 127–131.

(9) Li, G.; Shrotriya, V.; Yao, Y.; Yang, Y. Investigation of annealing effects and film thickness dependence of polymer solar cells based on poly(3-hexylthiophene). *J. Appl. Phys.* **2005**, *98*, 1–5.

(10) Jo, J.; Kim, S. S.; Na, S. I.; Yu, B. K.; Kim, D. Y. Time-dependent morphology ewolution by annealing processes on polymer:Fullerene blend solar cells. *Adv. Funct. Mater.* **2009**, *19* (6), 866–874.

(11) Dennler, G.; Scharber, M. C.; Brabec, C. J. Polymer-fullerene bulk-heterojunction solar cells. *Adv. Mater.* **2009**, *21*, 1323–1338.

(12) Zhao, J.; Swinnen, A.; Van Assche, G.; Manca, J.; Vanderzande, D.; Van Mele, B. Phase diagram of P3HT/PCBM blends and its implication for the stability of morphology. *J. Phys. Chem. B* **2009**, *113* (6), 1587–1591.

(13) Bliznyuk, V. N.; Hazel, J. L.; Wu, J.; Tsukruk, V. V. Quantitative Probing in Atomic Force Microscopy of polymer Surfaces. **1998**, 252–265.

(14) Li, G.; Shrotriya, V.; Yao, Y.; Huang, J.; Yang, Y. Manipulating regioregular poly(3-hexylthiophene) : [6,6]-phenyl-C61-butyric acid methyl ester blends—route towards high efficiency polymer solar cells. *J. Mater. Chem.* **2007**, *17*, 3126.

(15) De Villers, B. T.; Tassone, C. J.; Tolbert, S. H.; Schwartz, B. J. Improving the reproducibility of P3HT:PCBM solar cells by controlling the PCBM/ cathode interface. *J. Phys. Chem. C* **2009**, *113* (44), 18978–18982.

(16) Dante, M.; Dante, M.; Peet, J.; Peet, J.; Nguyen, T.-Q.; Nguyen, T.-Q. Nanoscale Charge Transport and Internal Structure of Bulk Heterojunction Conjugated Polymer/ Fullerene Solar Cells by Scanning Probe Microscopy. *J. Phys. Chem. C* **2008**, *112*, 7241.

(17) Eaton, P.; West, P. *Atomic Force Microscopy;* Oxford Univ. Press, Oxford, U.K., 2010.

(18) Greiner, M. T.; Chai, L.; Helander, M. G.; Tang, W. M.; Lu, Z. H. Metal/metal-oxide interfaces: How metal contacts affect the work function and band structure of MoO3. *Adv*. *Funct*. *Mater*. **2013**, *23* (2), 215–226.

(19) Guo, H.; Lin, N.; Chen, Y.; Wang, Z.; Xie, Q.; Zheng, T.; Gao, N.; Li, S.; Kang, J.; Cai, D.; et al. Copper nanowires as fully transparent conductive electrodes. *Sci. Rep*. **2013**, *3*, 2323–2330.

(20) Kang, H.; Sowade, E.; Baumann, R. R. Direct intense pulsed light sintering of inkjet-printed copper oxide layers within six milliseconds. *ACS Appl. Mater. Interfaces* **2014**, *6* (3), 1682–1687.

(21) Material Properties Data: Alumina (Aluminum Oxide) http://www.makeitfrom.com/material-properties/Alumina-Aluminum-Oxide-Al2O3 (accessed on Mar 11, 2016).

(22) Hermenau, M.; Riede, M.; Leo, K.; Gevorgyan, S. A.; Krebs, F. C.; Norrman, K. Water and oxygen induced degradation of small molecule organic solar cells. *Sol. Energy Mater. Sol. Cells* **2011**, *95* (5), 1268–1277.

# CHAPTER 4

# EXPERIMENTAL

## 4.1 Materials:

Commercially available regioregular- poly (3-hexylthiophene), P3HT with average molecular weight of 30,000 – 60,000 g/mol, purchased from Reiki Metals Inc. and was used as recieved. 1, 2-dichlorobenzene (99% pure), ammonium hydroxide (28% $NH_3$ in water), hydrogen peroxide (30% w/w), and calcium (beads) were purchased from Sigma Aldrich. Poly (3, 4-ethylenedioxythiophene) polystyrene sulfonate (PEDOT:PSS, M121 Al 4083) was obtained from Ossila Ltd. and stored in the refrigerator at 3-5 °C temperature. Phenyl-C61-butyric acid methyl ester (PCBM) was purchased from SES Research Ltd, and it was stored inside the glovebox under nitrogen atmosphere. Indium tin oxide (ITO) coated glass plates were purchased from SPI supplies with glass thickness of 1.1 mm and ITO layer thickness of 700 nm. Aluminum wire, tungsten filaments, tungsten boat, mask were used as received from R. D. Mathias.

## 4.2 General Device Making Procedure:

Device making procedure has been divided into number of subsections which are listed below.

1) Cleaning of ITO glass substrates.
2) Preparation of the active layer solution.
3) Spin Coating Procedure for PEDOT:PSS and the blend of P3HT:PCBM.
4) Deposition of electrodes by metal evaporation.

In a typical device fabrication method, ITO coated glass substrates were cleaned and UV treated. It was then immediately taken for PEDOT:PSS coating followed by

active layer coating using a spin coater. Substrates were solvent annealed and dried inside the glovebox and then taken for the deposition of a layer of calcium and aluminum.

### 4.2.1 Cleaning of ITO Glass Substrates

The first and most important task to do for any device fabrication process is to clean the substrates prior to the deposition of all other layers of a solar cell. Presence of dust and lint causes formation of uneven comet like structures along with pinholes on coated films. We have followed the cleaning procedure to remove any dust, organic, and inorganic substances present in a trace amount, which may affect the device performance. The ITO coated substrates typically have a sheet resistance of 8-12 Ohms/ sq. inch and a thickness of 1 mm. Coating of ITO layer on glass was ~700 nm, which was further confirmed by cross section analysis using SEM.

In a typical procedure, ITO coated glass substrates were first wiped with dichloromethane using a cotton bud. Then the substrates were washed with a soap solution gently rubbing with a soft brush. A hot solution of DI water (50 mL), 30% hydrogen peroxide (10 mL), and 28% ammonium hydroxide (10 mL) was prepared by heating to 60-70 °C. The substrates were placed in the hot solution keeping the ITO coated side up about 15 minutes. Substrates were then taken out and dipped in DI water in a glass jar for ultrasonication about 15 minutes. Substrates. After the ultrasonication, substrates were removed from the jar and subjected to dry under stream of nitrogen and placed in a cover box to perform UV cleaning using a UV cross-linker for 35 minutes. These UV cleaned devices were ready for coating next layers.

### 4.2.2 Preparation of the active layer solution

P3HT (12.5 mg) was charged with 350 µL 1, 2-dichlorobenzene in a 4 mL vial. 1, 2-dichlorobenzene was dried over magnesium sulfate prior to the addition. This solution was allowed to stir overnight (16 Hours) inside a glove box under nitrogen atmosphere at room temperature. To a separate 4 mL vial PCBM (10 mg) and 1, 2-dichlorobenzene (250 µL) were added inside the glove box. This solution was also allowed to stir overnight for 16 hours under same inert conditions. The solutions prepared in this manner were mixed together and allowed to stir for another 4 hours. Prior to the spin coating process, the blend solution was filtered using a 0.45 micron PVDF 12 mm syringe filter to a clean vial.

### 4.2.3 Spin Coating Procedure

#### 4.2.3.1 Coating PEDOT:PSS Layer

Spin coating process was performed under an anhydrous nitrogen atmosphere in a nitrogen-filled glove box. The pressure was maintained at 3" of water inside the glove box. Cleaned ITO coated glass substrate was kept in a slot provided on the chuck of spin coater. PEDOT: PSS solution was filtered using a 22 mm PVDF syringe filter. PEDOT:PSS solution (600 µL) was dispensed on the ITO coated glass substrates and the solution was spin coated at two different rotating speeds of 2000 rpm for 10 seconds and 5000 rpm for 60 seconds. The PEDOT.PSS coated substrate was placed on a hot plate immediately and annealed at 150 °C for 2 hours.

#### 4.2.3.2 Coating P3HT:PCBM Active Layer

PEDOT: PSS coated substrate was placed on a chuck of spin coater. Infra-red lamp at a height of 18 cm was placed on the top of the spin coater. An active layer solution (80 µL) was dispensed on the substrate. Infra-red lamp was then switched on

immediately and spin coater was set to the rotational speed of 2000 rpm for 250 seconds under IR heat. Then the active layer coated substrate was kept inside the glovebox for 5 minutes to dry prior to the solvent annealing process using 1, 2-dichlorobenzene solvent vapors.

In a typical solvent annealing process, a glass chamber was saturated with vapor of 1, 2-dichlorobenzene before placing the substrate. The substrate was kept on a stage inside the chamber for 7 minutes and followed by allowing to dry inside the glovebox.

### 4.2.4 Evaporation of Cathode Materials

After coating the active layer followed by solvent annealing process, substrates were coated with calcium and aluminum using a thermal evaporator. In order to pattern the device area, substrates were covered with vinyl masked with 3 rectangular cut openings to have the cell area of 7 mm X 1.5 mm for each cell. Substrate was mounted horizontally on the holder inside the thermal evaporator. Aluminum wires about 5-6 was loaded on a tungsten filament and 2-3 calcium beads were loaded on a molybdenum boat inside the evaporator. The deposition rate of 0.1 nm/sec and pressure of 1 X $10^{-5}$ Torr were maintained during the deposition of calcium layer to yield the layer thickness of ~5 nm.. A layer of aluminum was then deposited on the calcium layer by maintaining the deposition rate at 0.1 nm/sec with the pressure at 8 X $10^{-6}$ Torr. Figure 4.1 shows a substrate subjected to each fabrication steps of P3HT:PCBM based solar cells along with a final working device (see Figure 4.2).

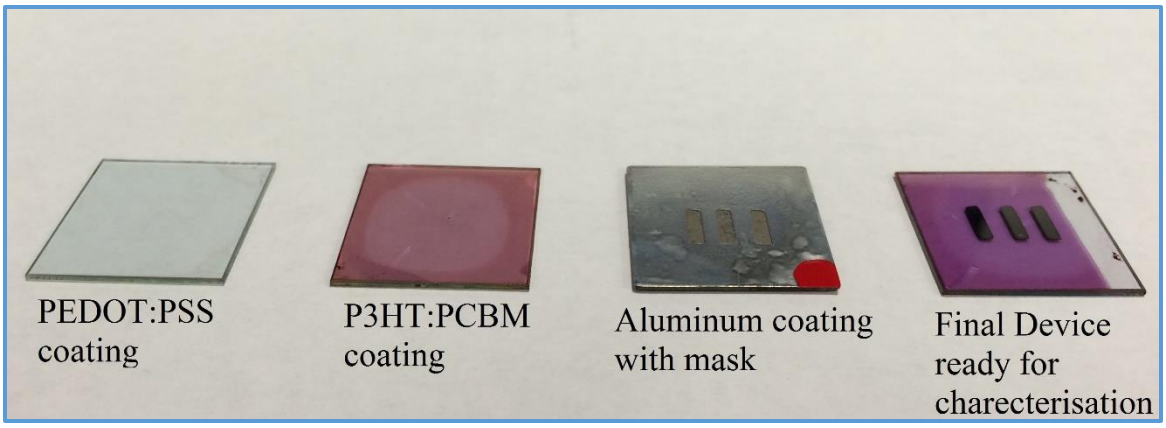


**Figure 4.1**: Device fabrication stages of a P3HT:PCBM BHJ solar cell

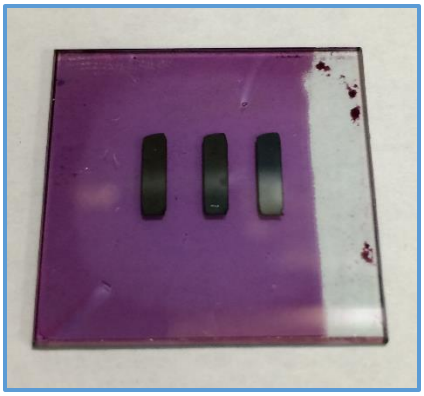

**Figure 4.2:** Final working device

### 4.3 Device Characterization:

The solar cells were characterized using a Keithley 2400 source meter equipped with a PC which used Labview program for obtaining the IV curves by sweeping the voltage from -1 to +1V range. The testing of the devices was performed in ambient conditions at room temperature using a solar simulator under xenon arc lamp of intensity of 100 mW/cm$^2$ which is 1 sun illumination and AM1.5G spectrum. The lamps intensity was calibrated with standard silicon solar cell of area 1 cm$^2$ purchased from Solarmade. Although Labview software directly measures fill factor, shunt resistance, open circuit

voltage, short circuit current and efficiency, these parameters were calculated manually after collecting the IV curve using following two equations.

1. $FF = \frac{J_{max} \times V_{max}}{J_{sc} \times V_{OC}}$

2. $PCE = \frac{J_{sc} \times V_{OC} \times FF}{P_{input}}$

Where,

FF = Fill factor

$J_{max}$ = Current density at maximum power output

$V_{max}$ = Voltage at maximum power output

$J_{sc}$ = Short circuit current density

$V_{oc}$ = Voltage at zero current

PCE = Power conversion efficiency

$P_{input}$ = Power input

**4.4 Estimation of the Conductivity of Evaporated Copper**

Glass plate with a surface area of 24.8 mm X 24.8 mm was wiped with a cotton swab dipped in dichloromethane. This plate was then mounted inside the evaporator on a sample holder. Copper beads (2 g, 99 % purity) was kept on molybdenum boat and loaded inside the thermal evaporator. Pressure inside the evaporator was allowed to build upto $10^{-6}$ Torr. For copper evaporation, parameters on the thermal evaporator controller were set to the density of 8.92 g/cm$^3$, and Z-factor at 0.438, to yield the final thickness of 100 nm. To start evaporation, power against the loaded boat was increased with power controller knob slowly in small steps to reach upto the point where copper beads melts and starts evaporating. Current gauge should reflect 200mA reading at this point. Evaporation rate was maintained at 0.3 nm/second and finally thickness of 100 nm can be achieved in 5 minutes and 50 seconds. Coated plate was taken out of the thermal

evaporator chamber and stuck with a mask with rectangular cut opening of 2 mm X 6 mm, kept for sputter coating of gold and palladium for two electrode contacts.

Sputter coating was performed with Emscope SC500 sputter coater. Substrate was kept on sample rim inside the vacuum chamber and maintained at pressure 0.13 Torr. Total current during coating applied was 12 mA and process was set for 4 cycles of 4 minutes each. Substrates were then taken for IV-measurement on Keithley 2400 sourcemeter. Two oppositely charged electrodes (probes) were connected to two ends of a substrate separated by 6 mm channel distance. These electrodes were connected to a Keithley 2400 sourcemeter equipped with a PC that has Labview to obtain the IV curve.

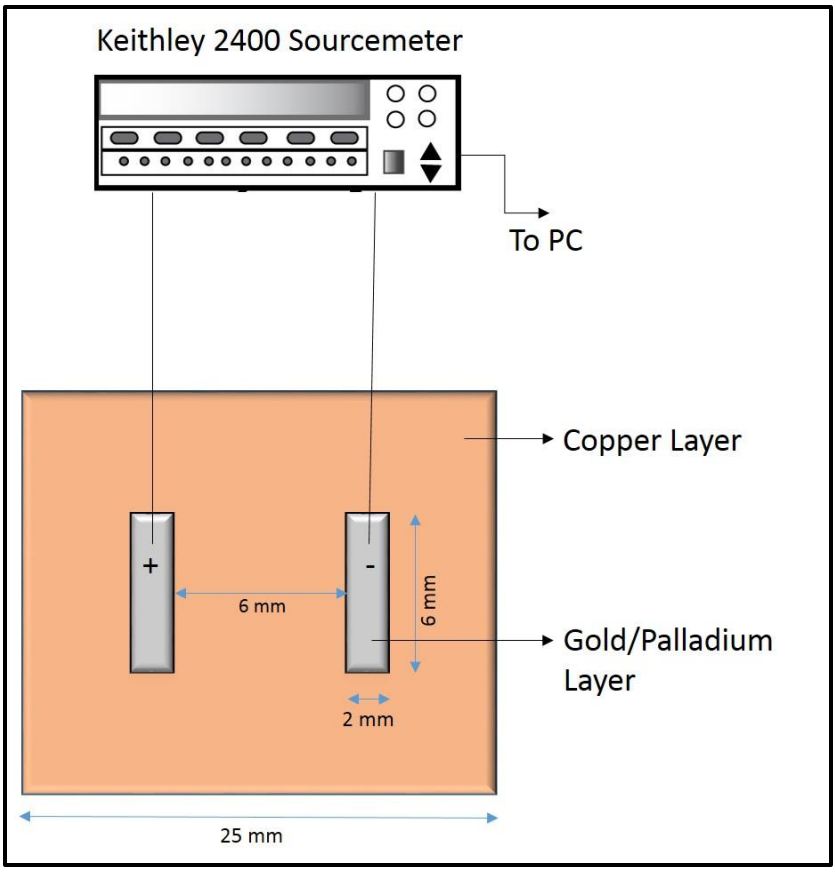


**Figure 4.3:** Schematic of metal conductivity measurement.

The schematic diagram of this arrangement is shown in Figure 4.3. Voltage was swept between -1.0 V to 1.0 V and current value was measured. From the I-V values, resistivity and conductivity values were calculated using following equations.

$$V = IR$$

$$\rho = \frac{R \times A}{l}$$

$$\sigma = \frac{1}{\rho}$$

Where,

R=Resistance

A=Area of cross section

l= distance between two electrodes on the plate.

$\rho$=*Resistivity*

$\sigma$=*Conductivity.*

**4.5 Fabrication of Large Scale Solar Cell**

Experimental is divided into three parts 1. Formulation of trial ink which was supposed to have similar properties in terms of viscosity, surface adhesion and fluidity on the plastic substrates. 2. Formation of a PEDOT:PSS layer and bulk heterojunction layer on ITO coated plastic substrates. 3. Formation of a cathode layer using copper nanoparticles ink (nanoink) using screen printing and further annealing using heat and intense pulse light (IPL) treatment.

### 4.5.1 Formulation of a Trial Ink

PEDOT: PSS from Sigma Aldrich for ink jet printing was procured and studied for viscosity parameters. These parameters calculated from viscometer and further matched with the trial ink flow parameters which are tabulated below in Table 4.1.

**Table 4.1:** Viscosity parameters of PEDOT: PSS for ink jet printing

| Viscosity (cP) | Percentage level (%) | Spindle no. | rpm |
|---|---|---|---|
| 54 | 90.4 | 61 | 100 |

Considering these parameters trial ink was formulated as 10% ethylene glycol, 2% food dye, 60% ethanol and 28% water. Formulated ink is then taken for ultrasonic spray coating on ITO coated plastic substrate which was polyethylene terephthalate (PET).

### 4.5.2 Deposition of a Trial Ink

Before formation of a bulk heterojunction layer, trials were to be done for trial ink, as to avoid use of the expensive materials such as PEDOT: PSS and active layer components such as P3HT. ITO coated PET substrate is then coated with trial ink using ultrasonic spray. Ultrasonic spray equipment works in synchronization with step motor, which moves the plastic substrate back and forth. Therefore, for uniform film formation, parameters for both step motor and ultrasonic spray controller needs to be synchronized. A syringe was loaded with trial ink and dispensed at steady rate to the ultrasonic spray nozzle. Simultaneously step motor parameters were set to move the stage back and forth. The homogeneity as well as uniformity over the surface of plastic was observed and

parameters were optimized accordingly. The best working parameters are tabulated in Table 4.2 for both the equipment.

**Table 4.2:** Step Motor and ultrasonic spray Parameters

| | Sr. No. | Parameter | Optimized value for uniform layer |
|---|---|---|---|
| **Step motor parameters** | 1 | Stage speed | 15 mm/sec |
| | 2 | Stage distance | 120 mm |
| | 3 | No. of passes | 4 |
| | 4 | Pause between each pass | 0 Sec |
| **Ultrasonic spray control panel parameters** | 1 | Flow Rate | 2 mL/min |
| | 2 | Jet Force | 40 Lit/min |
| | 3 | Conveyer | 3 Ft/min |
| | 4 | Nozzle power | 3 Watts |
| | 5 | Spray on | 1 inch |
| | 6 | Spray off | 1 inch |
| | 7 | Stage height | 10.6 cm |
| | 8 | Spray Width | 2 inch |

### 4.5.3 Deposition of PEDOT: PSS Layer on ITO Substrate.

After setting up the parameters for trial ink, PEDOT: PSS (483095 from Sigma Aldrich) was used for coating on ITO coated plastic substrates. ITO plates were cut in rectangular shape with dimensions 7 cm X 140 cm. Trials were performed for optimizing

the parameters for uniform transparent thin layer of PEDOT:PSS on ITO coated plastic substrates. These parameters mainly include flow rate, no. of passes, pause between each pass, and speed of motor. All these parameters were changed one by one which are shown in table number 4.4. Trials were done changing the main parameters such as speed of motor and nozzle power. Changing these two parameters showed significant change in the uniformity and homogeneity of the PEDOT: PSS layer. This has to be noted that after every 4 passes substrates were taken for annealing on hot plate for 5 minutes at 150°C. Flow rate of 2 mL/sec and deposition rate of 937 µg/sq. inch was maintained with ultrasonic spray controller.

**Table 4.4**: Ultrasonic spray parameters for uniform PEDOT: PSS layer

| Flow rate (mL/min.) | No. of passes | Pause between every 4 pass | Speed of motor (mm/sec) | Nozzle Power | Observation |
|---|---|---|---|---|---|
| 1 | 64 | 5 min. | 5 | 6 | More dense, big droplets |
| 1 | 64 | 5 min. | 10 | 6 | More dense, big droplets |
| 1 | 64 | 5 min. | 15 | 4 | Ok |
| 1 | 64 | 5 min. | 20 | 4 | Ok |
| 1 | 64 | 5 min. | 25 | 2 | Ok |
| 1 | 64 | 5 min. | 30 | 2 | Good |
| 1 | 64 | 5 min | 35 | 1 | Ok |
| 1 | 64 | 5 min. | 40 | 1 | Ok |

Height does have significant effect on the uniformity of coated layer. Keeping variables unchanged from Table 4.4 with motor speed 30 and nozzle power 2, substrate height from spray nozzle was changed. Height was varied from 3-20 cm and uniform film identified at 13 cm and this height was noted down with the present set of available parameters.

### 4.5.4 Deposition of P3HT and PDIB Silane as an active layer.

P3HT was weighed 500 mg and it was added in 20 mL of dichlorobenzene, stirred overnight until it dissolved. Similarly, perylene diimide bridged (PDIB) silane weighed 500 mg added in 20 mL of dichlorobenzene, stirred overnight until it is dissolved. Both the solutions are then mixed together and stirred for two hours. Ultrasonic spray coating unit is equipped with automatic syringe dispensing unit. The solution is then loaded in the 50 ml syringe which is connected to the ultrasonic spray nozzle. Following parameters gave the optimum results for active layer spray coating.

| | Sr. No. | Parameter | Optimized value for uniform layer |
|---|---|---|---|
| **Step motor parameters** | 1 | Stage speed | 30 mm/sec |
| | 2 | Stage distance | 140 mm |
| | 3 | No. of passes | 4 |
| | 4 | Pause between each pass | 0 Sec |
| **Ultrasonic spray control panel parameters** | 1 | Flow Rate | 1 mL/min |
| | 2 | Jet Force | 40 Lit/min |
| | 3 | Conveyer | 3 Ft/min |
| | 4 | Nozzle power | 6 Watts |
| | 5 | Spray on | 1 inch |
| | 6 | Spray off | 1 inch |
| | 7 | Stage height | 13.5 cm |
| | 8 | Spray Width | 2 inch |

Substrates after every 8 No. of passes were annealed at 100$^{O}$C and then allowed to cool for 5 min. and again passed through ultrasonic spray. After 56 no. of passes film appeared to be well formed and spread uniformly over the substrate. All the spray coating and annealing as well as cooling was done in ambient conditions.

### 4.5.6 Formation of Cathode Layer

#### 4.5.6.1 Screen Printing:-

After putting an active layer an electron collecting layer was deposited using screen printing method, for which copper nanoparticle paste (nano-ink) formulated in lab was used. This metal layer was deposited on an active layer using screen printing method. A 20 inch X 24 inch screen was taken and coated uniformly with blocking polymer. Allowed to dry for a day and then taken for UV curing. Stencil was made using graphics software and kept below the screen to block UV rays. UV curing formed a pattern on screen as same as blocking stencil pattern Figure 4.4.

**Figure 4.4:** Blocking stencil for screen printing

UV cured screen is then washed with water and blow dried with hot air. The screen with given pattern was used to print the cathode layer on the active layer. The

screen was then placed on the active layer coated substrate and nano-ink formulated with copper nanoparticles of size 5-nm diameter placed on the screen. Nano-ink was then placed on screen and dispersed with an applied pressure with the use of blade making a pattern on the active layer. Copper nano-particle paste formed a patterned shape on the active layer which was taken further for drying and intense pulse light (IPL) sintering.

#### 4.5.6.2 IPL Treatment

After forming a given pattern of nanoink on substrates, nanoink was dried using hot air oven kept at 100 °C for 10 minutes. Substrates were then taken for IPL treatment in which an intense pulsed light (IPL) from a xenon flash lamp was used to sinter copper nanoink printed on low temperature polymer substrates at room temperature in ambient condition. With the light wavelength from 200 to 1100 nm IPL treatment was carried out with three different parameters given below. Conductivity measurement was performed on cathode layer before and after IPL treatment by the method given in section 4.4. Parameters of IPL treatment performed on cathode layer are shown in Table 4.7.

**Table 4.7**: Intense pulse light sintering parameters

| Energy Applied | Time of exposure | Pulse width |
|---|---|---|
| 30 J/cm$^2$ | 10 sec | 2 ms |
| 40 J/cm$^2$ | 10 sec | 2 ms |
| 50 J/cm$^2$ | 10 sec | 2 ms |

# CHAPTER 5

# CONCLUSION AND FUTURE APPROACH

In conclusion, a novel solvent annealing method was developed to achieve high efficiency organic solar cells (P3HT: PCBM) with power conversion efficiency of 9.2%. It was found that the surface roughness of an active layer increased due to improved polymer crystal growth and PCBM cluster formation. The I-V characteristic of the solvent annealed devices shows reduced resistance and as a result improved current density. These results provide profound insight to photovoltaic mechanism in correlation with the active layer morphology upon the solvent treatment process. Our future work will concentrate on applying the similar solvent annealing technique for devices fabricating using other molecular systems.

In the effort of developing new cathode materials to replace highly unstable aluminum, we have successfully characterized these solar cells by replacing aluminum with copper. The P3HT:PCBM BHJ solar cells developed with copper exhibit comparable efficiency similar to that of with aluminum cathode. However, further studies need to be done to measure the lifetime and durability of these devices. Importantly, calcium metal is also used beneath the copper layer in these devices to match the LUMO energy level of PCBM for efficient charge transfer to the cathode.

Tandem architecture provides benefits in terms of improving light absorption and resolving photon loss during the charge transfer. Therefore, our future work will focus on exploring new tandem device architecture with the combination of metal oxides, organometallic compounds, and organic semiconducting materials.

Scalability studies show that there are significant improvements that can be done to obtain a working device. The present study only focused to obtain a uniform, homogenous layer using large-scale fabrication techniques rather than fabricating a final working device. Moreover, cathode copper nanoink compatibility was also analyzed during this thesis work. Cathode layer formed after screen-printing showed uniform and sharp pattern on the active layer. Copper nanoparticle dispersed nanoink layer showed improved performance in conductivity after sintering. Our future work will be focused on development of BHJ organic solar cell on large scale. With the nanoink layer and advanced sintering process developed here, the large scale manufacturing of organic solar cells is promising.